JM PAPERS

Thermoviscous localisation of volcanic eruptions is enhanced by variations in fissure width

Jesse J. Taylor-West[1] and Edward W. Llewellin[2]

[1]School of Mathematics, University of Bristol, Bristol BS81UG, UK
[2]Department of Earth Sciences, Science Labs, Durham University, Durham DH1 3LE, UK
Corresponding author: Jesse J. Taylor-West; Email: j.taylor-west@bristol.ac.uk

Volcanic fissure eruptions typically start with the opening of a linear fissure that erupts along its entire length, following which, activity localises to one or more isolated vents within a few hours or days. Localisation is important because it influences the spatiotemporal evolution of the hazard posed by the eruption. Previous work has proposed that localisation can arise through a thermoviscous fingering instability driven by the strongly temperature dependent viscosity of the rising magma. Here, we explore how thermoviscous localisation is influenced by the irregular geometry of natural volcanic fissures. We model the pressure-driven flow of a viscous fluid with temperature-dependent viscosity through a narrow fissure with either sinusoidal or randomised deviations from a uniform width. We identify steady states, determine their stability and quantify the degree of flow enhancement associated with localised flow. We find that, even for relatively modest variations of the fissure width ($< 10\,\%$), the non-planar geometry supports strongly localised steady states, in which the wider parts of the fissure host faster, hotter flow, and the narrower parts of the fissure host slower, cooler flow. This geometrically driven localisation differs from the spontaneous thermoviscous fingering observed in planar geometries and can strongly impact the localisation process. We delineate the regions of parameter space under which geometrically driven localisation is significant, showing that it is a viable mechanism for the observed localisation under conditions typical of basaltic eruptions, and that it has the potential to dominate the effects of spontaneous thermoviscous fingering in these cases.

Key words: magma and lava flow, nonlinear instability, pattern formation

1. Introduction

Basaltic fissure eruptions are the most common type of volcanic eruption on Earth (Sigurdsson 2000). Recent examples include the eruption of Kilauea's Lower East Rift

Zone (USA) in 2018 (Neal *et al.* 2019) and the ongoing sequence of eruptions on the Reykjanes Peninsular (Iceland) that began in 2021 (Troll *et al.* 2024). A fissure eruption occurs when a dyke – a magma-filled crack – intersects the Earth's surface, creating an elongated eruptive vent. The eruption typically onsets as a near-continuous curtain of lava fountaining, which localises over hours to days into discrete vents that produce isolated lava fountains and feed lava flows (e.g. Richter *et al.* 1970; Thorarinsson *et al.* 1973; Delaney & Pollard 1982; Eibl *et al.* 2017). The hazard posed by a fissure eruption evolves as the fissure localises; in particular, the path taken by fissure-fed lava flows is strongly influenced by the vent location (Rongo *et al.* 2016). Understanding the spatio-temporal evolution of a localising fissure eruption is, therefore, an important practical goal for the management of eruption hazards, as well as a problem of fundamental fluid dynamic interest.

Localisation is thought to arise from a thermoviscous instability, analogous to classical Saffmann–Taylor viscous fingering, by which hot, low-viscosity magma displaces cooled, higher viscosity fluid. The system becomes unstable to the formation of fingers of lower viscosity fluid (Pearson, Shah & Vieira 1973; Whitehead & Helfrich 1991; Helfrich 1995; Wylie & Lister 1995; Morris 1996; Wylie *et al.* 1999) which become preferred transport pathways that feed localised flow. Bruce & Huppert (1989) suggested that the localisation process could be driven by a feedback between solidification at the walls and the resulting effect on heat advection through the fissure due to the evolving fissure geometry. However, Wylie *et al.* (1999) argued that the localisation that occurs via this feedback evolves on a longer time scale than the localisation caused by thermoviscous fingering, making the latter the dominant effect. Other work has explored the potential role of other processes in localisation, including dynamic wall rock deformation (Ida 1992), drain-back of erupted lava (Jones *et al.* 2017), formation of plumes of decoupled bubbles of magmatic gas (Pioli *et al.* 2017; Houghton *et al.* 2021) and convective exchange flow within the dyke (Jones & Llewellin 2021).

Previous work on thermoviscous localisation has made the simplifying assumption that magmatic dykes have walls that are initially planar and parallel. However, dyke emplacement involves pulsatory, stochastic failure of heterogeneous country rock (Allgood *et al.* 2024), resulting in dykes that vary substantially in thickness along their length (Daniels *et al.* 2012; Parcheta *et al.* 2015). In this study, we explore the role that the non-planar geometry of dyke walls plays in localisation. We consider the flow of a viscous fluid with temperature-dependent viscosity through a dyke with variations in thickness along its length (i.e. the gap thickness varies perpendicular to the main flow direction; see figure 1). The full equations are reduced, taking advantage of the small aspect ratio of fissure width to length, as well as a number of additional physical assumptions, given in § 2. Furthermore, we employ a heat balance approach, detailed in § 2.1, to account for the temperature and viscosity field when averaging across the fissure width. A similar averaging approach has been used in a number of studies concerning cooling lava flows (Balmforth, Craster & Sassi 2004; Bernabeu, Saramito & Smutek 2016; Thorey & Michaut 2016; Hyman, Dietterich & Patrick 2022; Moyers-Gonzalez *et al.* 2023), as it maintains the key structure of the across-flow temperature profile in the model, while providing the numerical efficiency of averaging over the thin dimension of the flow. We first quantify behaviour in a dyke with sinusoidally varying width, constraining the role of amplitude and wavelength of the variation, and of the pressure difference driving the flow. We find that, under volcanologically relevant conditions, the thermoviscous fingering instability can be overprinted by the effect of geometry, which focusses hotter, faster flow into the wider portions of the dyke, and cooler, slower flow into the narrower portions. We then demonstrate the importance of this localisation mechanism in a more realistic
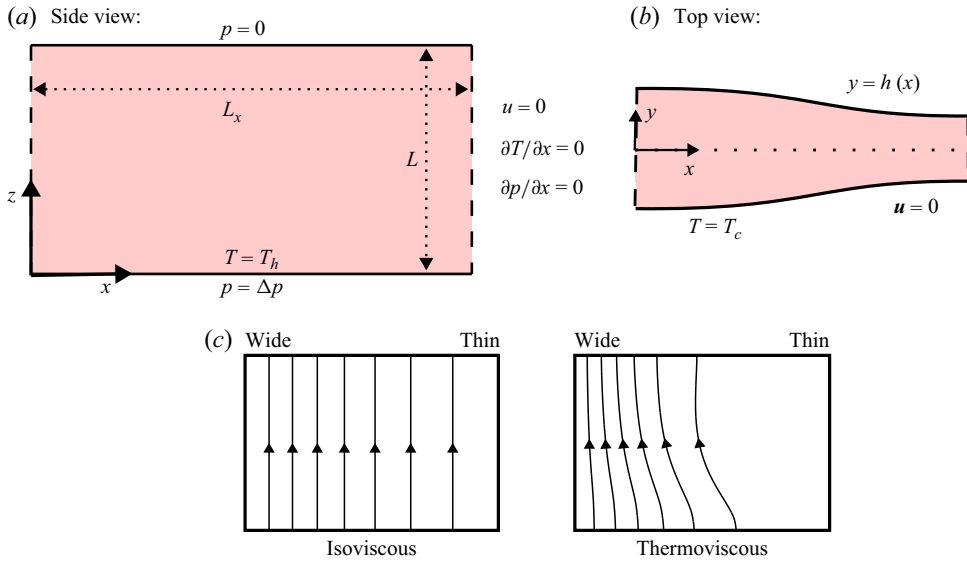
Figure 1. (*a,b*) Schematic of fissure geometry, coordinate system and boundary conditions. In the side view, panel (*a*), the bottom and top boundaries are the inflow and outflow, respectively, the dashed lines indicate no flux (symmetry) boundaries, and the double-headed arrows indicate the vertical and along-fissure length scales. In the top view, panel (*b*), the bottom and top boundaries are the side walls of the fissure, the dashed lines indicate no flux (symmetry) boundaries, and the dotted line indicates the assumed plane of symmetry down the centreline of the fissure. (*c*) Diagram indicating the effect that thermoviscosity has on the streamlines of volume flux in such a geometry. For an isoviscous fluid and the topography aligned with the flow direction, the streamlines are parallel. When the viscosity depends on temperature, the streamlines are diverted and flux is concentrated more strongly in the wider region of the fissure.

dyke geometry, consistent with field observations (Parcheta *et al.* 2015) and country-rock fracture patterns (Brodsky, Kirkpatrick & Candela 2016).

2. Problem definition

We consider a viscous fluid flowing through a narrow fissure. Figure 1(*a,b*) shows a diagram of the fissure geometry. We define a coordinate system such that z measures distance up the fissure in the (vertical) primary flow direction, y measures distance across the narrow dimension of the fissure and x measures distance along the fissure. The fissure height is L and its half-width varies via a prescribed dependence, $h(x, z)$, with a typical value of $h_0 \ll L$. We will consider the width to be independent of z and, in particular, predominantly impose a sinusoidal variation of the half-width,

$$h(x) = h_0 \left(1 + A \cos \left(\frac{2\pi x}{\lambda L} \right) \right), \tag{2.1}$$

where λ is the wavelength of the variation, non-dimensionalised by L. The independence of h on z is not a requirement of the model and, in practice, there is likely to be some variation in this direction; however, we anticipate that variations in the x-direction will couple most strongly with the advection of heat and, therefore, be most significant in driving flow localisation. For the sinusoidally varying geometry, the horizontal section considered in the model is of length $L_x = \lambda L/2$, such that a single half-wavelength fits inside the domain. The assumption of symmetry boundary conditions then restricts to symmetrical solutions that are periodic with the same wavelength as the geometry.

1015 A18-3

Figure 1(*c*) shows the effect of thermoviscosity for the flow through such a geometry, with topography aligned with the (vertical) pressure gradient. For an isoviscous fluid, the streamlines would remain aligned in the vertical direction, with a flux that varies with the cube of the local width, as per Darcy flow. For a temperature-dependent viscosity, however, the viscosity gradients arising from differential cooling drive the streamlines away from the thinner region and towards the wider region of the fissure. This provides the essential mechanism by which localisation is enhanced.

Neglecting viscous heating and thermal expansion, and making the lubrication approximation, the governing equations for the temperature, T, pressure (modified to include the hydrostatic contribution), p, and velocity, $\boldsymbol{u} = (u, v, w)$, are given to leading order by (cf. Wylie & Lister 1995)

$$\rho c_p \left(\frac{\partial T}{\partial t} + \boldsymbol{u} \cdot \boldsymbol{\nabla} T \right) = k \nabla^2 T, \tag{2.2}$$

$$\frac{\partial p}{\partial y} = 0, \quad \boldsymbol{\nabla}_2 p = \frac{\partial}{\partial y} \left(\mu(T) \frac{\partial \boldsymbol{u}_2}{\partial y} \right), \tag{2.3}$$

$$\boldsymbol{\nabla} \cdot \boldsymbol{u} = 0, \tag{2.4}$$

where ρ is the fluid density, c_p is the specific heat capacity, $k \equiv \rho c_p \kappa$ is the thermal conductivity, $\mu(T)$ is the temperature-dependent viscosity, specified later, and $\boldsymbol{u}_2 = (u, 0, w)$ and $\boldsymbol{\nabla}_2 = (\partial_x, 0, \partial_z)$ are the velocity and gradient in the plane of the fissure. These equations represent conservation of heat, conservation of momentum and incompressibility, respectively.

Figure 1 shows the prescribed boundary conditions on the temperature, T, pressure, p, and velocity, $\boldsymbol{u}$. The fluid is assumed to enter at a hot source temperature, T_h, and with a prescribed pressure, $\Delta p > 0$, at $z = 0$. At $x = 0$ and $x = L_x$, we assume symmetry conditions, $u = \partial p / \partial x = \partial T / \partial x = 0$. At the outflow, $z = L$, the pressure is atmospheric, $p = 0$. We assume no-slip, $\boldsymbol{u} = 0$, and a fixed cold temperature, $T = T_c$, on the fissure walls, $y = \pm h$. While this fixed temperature boundary condition is a significant simplification of the full thermodynamic conditions at the fissure walls, it is chosen for simplicity and consistency with previous work on the problem (Helfrich 1995; Wylie & Lister 1995; Morris 1996; Wylie *et al.* 1999). Similarly, for comparison to previous work, we assume an exponential dependence of viscosity on temperature

$$\mu = \mu_0 \exp\left(-\beta \left(T - T_0 \right) \right), \tag{2.5}$$

where T_0 and μ_0 are a reference temperature and viscosity, and β is a parameter that measures the strength of the dependence. This model, which has been used in previous fluid dynamical modelling of thermoviscous localisation, has also been proposed to capture the viscosity of molten basalt as a function of temperature in a number of other studies (Shaw 1969; Spera, Yuen & Kirschvink 1982; Dragoni 1989). More commonly, this dependence is parametrised by an Arrhenius viscosity law (McBirney & Murase 1984), $\mu = \mu_\infty \exp(B/T)$, sufficiently far from the glass transition, or via the Vogel–Fulcher–Tammann (VFT) equation (Giordano, Russell & Dingwell 2008), $\mu = \mu_\infty \exp(B/(T - T_g))$, when nearer the glass transition (at $T = T_g$). In any case, the exponential viscosity dependence (2.5) can be viewed as a linearisation of the argument of the exponential in a general dependence of the form $\mu = \exp(f(T))$, by writing $T = T_0 + (T - T_0)$ and assuming $T - T_0$ small (compared with T_0 in the case of the Arrhenius law or compared with $T_0 - T_g$ in the case of the VFT equation).

Dimensionless parameter	Symbol and definition
Pressure drop	$\Pi = \Delta p h_0^4/(\kappa \mu_h L^2)$
Viscosity parameter	$\gamma = \log(\mu_c/\mu_h)$
Amplitude of width variation	A
Wavelength of width variation	λ
Lateral extent of domain	L_x
Dimensionless quantity	Symbol and definition
Vertical flux	$q_z(x, z) = 2\int_0^h w \, dy$
Cross channel average temperature	$\mathcal{T}(x, z) = 1/h \int_0^h T \, dy$
Flux per unit length	$Q = 1/L_x \int_0^{L_x} q_z \, dx$
Surface flux ratio	$Q_r = \max_x\{q_z(x, z=1)\}/\min_x\{q_z(x, z=1)\}$
Scaled surface flux ratio	$\tilde{Q}_r = (1-A)^3 Q_r/(1+A)^3$

Table 1. Definition of dimensionless parameters and evaluated quantities.

Following Wylie & Lister (1995), we introduce dimensionless variables via

$$\hat{t} \equiv \frac{\kappa}{h_0^2}t, \quad \hat{y} \equiv \frac{y}{h_0}, \quad (\hat{x}, \hat{z}) \equiv \frac{1}{L}(x, z), \quad (\hat{u}, \hat{w}) \equiv \frac{h_0^2}{\kappa L}(u, w), \quad \hat{v} \equiv \frac{h_0}{\kappa}v, \quad \hat{p} \equiv \frac{p}{\Delta p}, \tag{2.6}$$

$$\hat{T} \equiv \frac{T - T_c}{T_h - T_c}, \quad \hat{\mu}(\hat{T}) \equiv \frac{\mu(T)}{\mu_h} = \exp(\gamma(1 - \hat{T})), \quad \hat{h} \equiv \frac{h}{h_0}, \tag{2.7}$$

where $\mu_h = \mu(T_h)$ (similarly, we define $\mu_c = \mu(T_c)$) and $\gamma = (T_h - T_c)\beta$. For the sinusoidal geometry, the dimensionless half-width is given by $\hat{h} = 1 + A\cos(2\pi\hat{x}/\lambda)$. After non-dimensionalising, the lateral extent of the domain is $\hat{L}_x = L_x/L$. The one difference here from the scalings adopted by Wylie & Lister (1995) is that we have scaled the pressure by Δp, rather than $\kappa \mu_h L^2/h_0^4$. The result is that a dimensionless pressure drop,

$$\Pi = \frac{\Delta p h_0^4}{\kappa \mu_h L^2}, \tag{2.8}$$

appears in our governing equations, rather than in the boundary condition for $\hat{p}$. We make the same assumptions of large Péclet number, $Pe \equiv \Delta p h_0^3/\kappa \mu_h L \gg 1$, and large Prandtl number, $Pr \equiv \mu_h/\rho\kappa \gg 1$. In using the lubrication approximation (2.3), we have assumed a small aspect ratio, $\epsilon \equiv h_0/L \ll 1$, and negligible inertia, which requires that the modified Reynolds number is small, $\epsilon Re \equiv \epsilon\rho\Delta p h_0^3/\mu_h^2 L \ll 1$. A further assumption required in our non-uniform geometry is that $\lambda \gg \epsilon$, which ensures the length scale of variations in the x-direction remains significantly larger than the cross-channel length scale. At leading order, after dropping hats on all dimensionless variables, the dimensionless governing equations are

$$\frac{\partial T}{\partial t} + \boldsymbol{u}_2 \cdot \boldsymbol{\nabla}_2 T + v\frac{\partial T}{\partial y} = \frac{\partial^2 T}{\partial y^2}, \quad \frac{\partial}{\partial y}\left(\mu(T)\frac{\partial \boldsymbol{u}_2}{\partial y}\right) = \Pi\boldsymbol{\nabla}_2 p, \quad \boldsymbol{\nabla}_2 \cdot \boldsymbol{u}_2 + \frac{\partial v}{\partial y} = 0, \tag{2.9}$$

where $p = p(x, z)$. Table 1 lists the key dimensionless parameters of the model and the dimensionless quantities we later report for our solutions.

For parameter values appropriate for a typical Hawaiian fissure eruption, we take: thermal diffusivity $\kappa \approx 5 \times 10^{-7}$ m^2 s^{-1} (Kilburn 2000); cross-channel length scale of $h_0 \approx 0.25$ m (Walker 1986); fissure height of $L \approx 1$ km (e.g. Anderson *et al.* 2024); and initial viscosity, $\mu_h \approx 300$ Pa s (Soldati, Houghton & Dingwell 2021). The pressure drop, Δp, arises primarily from the difference between the lithostatic pressure of the country rock and the hydrostatic pressure of the magma at the depth of the source. Taking the density of the country rock to be 2500 kg m^{-3} (Moore 2001) and the (vesicular) basaltic magma to have a density of 1500 kg m^{-3}, this gives $\Delta p \approx 10^7$ Pa for a source depth of 1 km, which is a feasible depth for the shallow crustal reservoirs that are thought to feed many fissure eruptions (e.g. Anderson *et al.* 2024). At this pressure drop, and the physical quantities assumed previously, we have $\epsilon = 2.5 \times 10^{-4} \ll 1$, $\epsilon Re = 4 \times 10^{-4} \ll 1$, $Pe = 1 \times 10^6 \gg 1$ and $Pr = 6 \times 10^5 \gg 1$, all satisfying the assumptions in the reduction of the governing equations. A typical value of the dimensionless pressure drop is around $\Pi = 260$, though this is likely to vary throughout an eruption, in particular reducing from a large value at the beginning of an eruption to a smaller value as the eruption wanes. An alternative scaling argument instead relies on observations of typical eruptive fluxes and an inference of the corresponding driving pressure drop (e.g. see Delaney & Pollard 1982). Tilling *et al.* (1987) report estimates of erupted lava volumes over given time periods during the 1972–1974 Mauna Ulu eruption of Kilauea volcano. These estimates only provide a rough estimate of instantaneous eruptive rates and are likely lower bounds since they are based on lava volume remaining on the surface, excluding material that drained back into the fissures before the eruption ended. Nonetheless, from these figures, we can obtain a typical flux of between 0.001 and 0.05 m^3 s^{-1} per metre length of fissure. This becomes non-dimensionalised by the scale $\kappa L / h_0 \approx 0.002$ m^2 s^{-1} to obtain values of the dimensionless flux per unit length, Q, between 0.5 and 25. Later, we will show that this typical range of Q is indeed spanned by the results of the study and corresponds to dimensionless pressure drops roughly in the range $150 < \Pi < 350$. Rescaling for the dimensional pressure drop, $\Delta p = \kappa \mu_h L^2 \Pi / h_0^4$, this gives 6×10^6 Pa $\lesssim \Delta p \lesssim 1.3 \times 10^7$ Pa, which is consistent with the above mentioned pressure scale estimate.

2.1. *Cross-fissure averaging*

As evidenced by (2.9), the evolution of the temperature profile across the fissure remains important to the dynamics, in particular, modifying the velocity profile across the channel. This feature is treated in different ways by Helfrich (1995) and by Wylie & Lister (1995) and Morris (1996). Wylie & Lister (1995) and Morris (1996) solved for the temperature and velocity fields across the fissure explicitly, maintaining the full effect of the cross-channel structure. They were able to do this efficiently in the uniform channel geometry because the problem becomes independent of x, and thus reduces to a two-dimensional problem in the $y-z$ plane. Wylie & Lister (1995) further showed that three-dimensional steady states arising from the fingering instability, or due to a channel of non-uniform width, can be obtained from the two-dimensional steady state in a uniform channel. This is possible since along streamlines of the average flow field, the evolution of the cross-channel steady-state temperature profile can be mapped onto the down-channel evolution of the two-dimensional problem. This provides a method of finding non-uniform steady states without approximation; however, the time derivative in the temperature equation cannot be treated in the same manner and so this approach is unable to accurately calculate time-dependent states. For the purposes of searching for non-uniform steady states by time-stepping, Wylie & Lister (1995) introduced a pseudo-time, but were unable to find any such steady solutions near the onset of the instability, instead observing that these

unstable solutions appeared to continue to evolve back onto the uniform steady solution branch, at a higher flux.

In contrast, Helfrich (1995) averaged the viscosity, velocity and temperature across the gap, assuming a parabolic 'Darcy' flow profile for the velocity at a viscosity set by the average temperature and approximating the across-channel temperature profile by a single sine mode in determining the heat flux to the walls. While the qualitative results were the same (regarding multiplicity of steady states and the onset of the fingering instability), there was significant quantitative discrepancy due to the averaging. In particular, there is a region of the flow field in which the true temperature profile takes the form of a core region at the source temperature, $T = 1$, and a boundary layer at the wall in which the temperature decreases to the wall temperature, $T = 0$. This results in a larger heat flux to the walls than predicted by the averaged model of Helfrich (1995), and also a region of significantly enhanced viscosity at the walls, which alters the velocity profile substantially. Nonetheless, this averaging allowed for efficient calculation in the two dimensions in the plane of the fissure, providing the nonlinear evolution of the unstable non-planar perturbations associated with the fingering instability. Helfrich (1995) also encountered numerical difficulties in integrating towards non-uniform steady states after the onset of the fingering instability, but unlike Wylie & Lister (1995), their solutions seemed to be approaching such states before the onset of numerical instability, leading them to conclude that the finite-amplitude fingered states are stable. In § 3.1, we revisit the uniform geometry, showing that both behaviours suggested by Wylie & Lister (1995) and Helfrich (1995) (namely continued evolution onto the high-flux uniform solution branch, or establishment of stable, steady, non-planar solutions) can occur.

For treating the cross-temperature profile, we take an approach between the above mentioned two, making an assumption for the functional form of the cross-channel temperature profile, and then integrating over y to obtain a consistent averaging of the momentum and heat equations. This approach follows the 'skin-theory' of Balmforth *et al.* (2004) for a cooling shallow viscoplastic dome (in our case, in the absence of the yield stress). Similar approaches are also used by Bernabeu *et al.* (2016), Thorey & Michaut (2016), Hyman *et al.* (2022) and Moyers-Gonzalez *et al.* (2023) in the modelling of cooling lava flows. This has the computational advantages of reducing the problem to two dimensions, while treating the time evolution consistently (unlike the averaging of Wylie & Lister 1995) and capturing the effect of cross-channel viscosity variations more accurately than the averaging of Helfrich (1995). A comparison to these alternative averaging methods is made in Appendix B.

Specifically, we approximate the cross-channel temperature profile as consisting of a thermal boundary layer of width, $\delta(x, z)$, at the wall, over which the temperature varies quadratically from the value at the centreline, $T(x, 0, z) \equiv \Theta(x, z)$, to the wall temperature, $T = 0$. The variables δ and Θ are not independent, since the hot core remains at source temperature until the thermal boundary layers extends over the width of the channel and so $\Theta = 1$ if $\delta < h$, and $\delta = h$ if $\Theta < 1$. The cross-channel temperature profile is therefore approximated by

$$T(x, y, z) = \begin{cases} \Theta & \text{for } 0 \leqslant y < h - \delta, \\ \Theta \left(1 - \left(1 - \dfrac{h - y}{\delta} \right)^2 \right) & \text{for } h - \delta \leqslant y \leqslant h, \end{cases} \tag{2.10}$$

and T defined in $-h \leqslant y \leqslant 0$ by symmetry. The suitability of this approximation is supported by a comparison to temperature profiles arising in the unaveraged model of

Morris ([1996](#)), shown in figure 13(*b*). Since δ and Θ are not independent, we can introduce a single variable capturing the temperature field (cf. Balmforth *et al.* [2004](#)),

$$
\mathcal{E} \equiv \int_0^h (1 - T)\mathrm{d}y = \delta \left(1 - \frac{2}{3}\Theta\right) = \begin{cases} \dfrac{1}{3}\delta & \text{for } \delta < h,\ \Theta = 1, \\[2mm] h\left(1 - \dfrac{2}{3}\Theta\right) & \text{for } \delta = h,\ \Theta < 1. \end{cases} \tag{2.11}
$$

Thus, the variable $\mathcal{E}$ measures (half) the loss of dimensionless heat energy per unit area at a given point (x, z), compared with at the inlet, $z = 0$, and takes the value 0 when the fluid is at the hot, source temperature across the width of the channel, and the value h when the fluid is at the cooled, wall temperature across the width of the channel. We can invert the relationship (2.11) to relate δ and Θ to $\mathcal{E}$ via

$$
\delta = \min(3\mathcal{E}, h), \quad \Theta = \min\left(\frac{3(h - \mathcal{E})}{2h}, 1\right). \tag{2.12}
$$

Another natural variable to define for interpretation is the cross-channel average temperature, $\mathcal{T}$, which relates to the other variables via

$$
\mathcal{T} \equiv \frac{1}{h}\int_0^h T\mathrm{d}y = 1 - \frac{\mathcal{E}}{h} = \begin{cases} 1 - \dfrac{1}{3h}\delta & \text{for } \delta < h,\ \Theta = 1, \\[2mm] \dfrac{2}{3}\Theta & \text{for } \delta = h,\ \Theta < 1. \end{cases} \tag{2.13}
$$

Integrating (2.9*b*) twice, we obtain

$$
\boldsymbol{u}_2 = -\Pi \left(\int_y^h \frac{\hat{y}}{\mu(T)}\,\mathrm{d}\hat{y}\right)\boldsymbol{\nabla}_2 p, \tag{2.14}
$$

taking the divergence, substituting for the temperature dependent viscosity (2.5) and the temperature ansatz (2.10), and integrating over $-h \leqslant y \leqslant h$ gives

$$
\boldsymbol{\nabla}\cdot\boldsymbol{q} \equiv 2\Pi\boldsymbol{\nabla}\cdot(\mathcal{L}\boldsymbol{\nabla}p) = 0, \tag{2.15}
$$

where we have defined the flux, $\boldsymbol{q} \equiv 2\Pi\mathcal{L}\boldsymbol{\nabla}p$, and we have now dropped the subscript 2 from the in-plane gradient since we will consider all gradients to be in the plane of the fissure from now on. The flux factor,

$$
\mathcal{L}(x, z) \equiv -\int_0^h \int_y^h \frac{\hat{y}}{\mu(T)}\,\mathrm{d}\hat{y}\,\mathrm{d}y \tag{2.16}
$$

$$
= -\delta^3 \exp(-\gamma(1 - \Theta))\left(\left(\frac{h}{\delta} - 1\right)^2 I_0 + 2\left(\frac{h}{\delta} - 1\right) I_1 + I_2 + \frac{1}{3}\left(\frac{h}{\delta} - 1\right)^3\right), \tag{2.17}
$$

where the I_k terms are given by integrals,

$$
I_k \equiv \int_0^1 \eta^k \exp(-\gamma\Theta\eta^2)\,\mathrm{d}\eta, \tag{2.18}
$$

which in turn can be evaluated analytically or in the form of error functions (cf. Balmforth *et al.* [2004](#)). When $\delta \to 0$ and $\Theta = 1$, this reduces to $\mathcal{L} \to -h^3/3$, which corresponds to $\boldsymbol{q}$ being given by Darcy's law at the inlet viscosity $\mu(1) = 1$, and when $\delta = h$ and $\Theta = 0$, we find $\mathcal{L} = -\exp(-\gamma)h^3/3$, corresponding to Darcy flux at the final viscosity, $\mu(0) = \exp(\gamma)$. Thus, the flux captures the expected results for the isothermal cases.

Following Balmforth *et al.* (2004), we now integrate the heat equation over the thermal boundary layer $h - \delta \leqslant y \leqslant h$, obtaining a nonlinear conservation equation for $\mathcal{E}$,

$$\frac{\partial \mathcal{E}}{\partial t} + \Pi \nabla \cdot (\mathcal{S} \nabla p) = \mathcal{C}. \tag{2.19}$$

The right-hand side of (2.19), $\mathcal{C} \equiv 2\Theta/\delta$, is a source term arising from cooling at the walls, while the flux of $\mathcal{E}$, $\Pi \mathcal{S} \nabla p$, involves the nonlinear factor, $\mathcal{S} \equiv \mathcal{U}\mathcal{E} - \mathcal{G}$, which contains a term due to advection, $\mathcal{U}\mathcal{E}$, and a term arising from the vertical structure of the temperature field, $-\mathcal{G}$. The functions $\mathcal{U}$ and $\mathcal{G}$ are given by

$$\mathcal{U} = -\delta^2 \exp(-\gamma(1 - \Theta)) \left(\left(\frac{h}{\delta} - 1 \right) I_1 + I_2 \right), \tag{2.20}$$

$$\mathcal{G} = -\frac{1}{3} \delta^3 \Theta \exp(-\gamma(1 - \Theta)) \left(\left(\frac{h}{\delta} - 1 \right) I_1 + I_2 - \left(\frac{h}{\delta} - 1 \right) I_3 - I_4 \right). \tag{2.21}$$

Since we view δ and Θ as functions of $\mathcal{E}$ (via (2.12)), all of the terms $\mathcal{L}, \mathcal{C}, \mathcal{U}$ and $\mathcal{G}$ (and hence $\mathcal{S}$) are functions of $\mathcal{E}$ (and the imposed $h(x)$). To summarise, we have the following system of equations for the unknown fields, $\mathcal{E}$ and p:

$$\frac{\partial \mathcal{E}}{\partial t} + \Pi \nabla \cdot (\mathcal{S}(\mathcal{E}) \nabla p) = \mathcal{C}(\mathcal{E}), \quad \nabla \cdot (\mathcal{L}(\mathcal{E}) \nabla p) = 0, \tag{2.22}$$

$$\mathcal{C}(\mathcal{E}) = \frac{2\Theta(\mathcal{E})}{\delta(\mathcal{E})}, \quad \delta(\mathcal{E}) = \min(3\mathcal{E}, h), \quad \Theta(\mathcal{E}) = \min\left(\frac{3(h - \mathcal{E})}{2h}, 1 \right), \tag{2.23}$$

$$\mathcal{L}(\mathcal{E}) = -\delta^3 \exp(-\gamma(1 - \Theta)) \left(\left(\frac{h}{\delta} - 1 \right)^2 I_0 + 2 \left(\frac{h}{\delta} - 1 \right) I_1 + I_2 + \frac{1}{3} \left(\frac{h}{\delta} - 1 \right)^3 \right), \tag{2.24}$$

$$\mathcal{S}(\mathcal{E}) = \mathcal{U}(\mathcal{E})\mathcal{E} - \mathcal{G}(\mathcal{E}), \quad \mathcal{U}(\mathcal{E}) = -\delta^2 \exp(-\gamma(1 - \Theta)) \left(\left(\frac{h}{\delta} - 1 \right) I_1 + I_2 \right), \tag{2.25}$$

$$\mathcal{G}(\mathcal{E}) = -\frac{1}{3} \delta^3 \Theta \exp(-\gamma(1 - \Theta)) \left(\left(\frac{h}{\delta} - 1 \right) I_1 + I_2 - \left(\frac{h}{\delta} - 1 \right) I_3 - I_4 \right), \tag{2.26}$$

$$I_k \equiv \int_0^1 \eta^k \exp(-\gamma \Theta \eta^2) \, \mathrm{d}\eta, \tag{2.27}$$

with boundary conditions

$$\begin{cases} \mathcal{E} = 0 \quad \text{and} \quad p = 1 & \text{at} \quad z = 0, \\ p = 0 & \text{at} \quad z = 1, \\ \partial p / \partial x = \partial \mathcal{E} / \partial x = 0 & \text{at} \quad x = 0, \ L_x. \end{cases} \tag{2.28}$$

Thus, (2.22) constitutes a nonlinear hyperbolic equation for $\mathcal{E}$ with an elliptic constraint on p. The remaining, algebraic, equations simply relate the nonlinear terms to the temperature field via $\mathcal{E}$. We discretise the spatial dependence of this system via a finite volume scheme, with upwinded fluxes in the z-direction, and we time step using a fourth-order, five-stage

Rosenbrock method (Roche 1987). Further details of the numerical method are given in Appendix A. Steady-state solutions are obtained either by natural continuation in Π or by pseudo-arclength continuation. In the former, we start from a large value of Π (say $\Pi = 400$), where a temperature distribution close to the inlet temperature, $\mathcal{E} \approx 0$, is a good initial guess. Having obtained an initial solution, we then decrease Π in steps, using the previous solution as an initial guess for solving the nonlinear steady-state problem directly (i.e. by Newton iteration). If the direct solve fails, we time step to a steady state. With pseudo-arclength continuation (e.g. see Allgower & Georg 2003), we do not impose the step in Π, but solve for a new steady state with an additional constraint that the new solution is a prescribed small distance along the solution curve from the previous one. This approach can capture fold bifurcations and unstable solution branches.

The systems studied by Helfrich (1995) and Wylie & Lister (1995) can be couched in the same manner as ours. For the Darcy averaging of Helfrich (1995), we can let $\mathcal{E}$ be instead defined by the difference between the average temperature across the fissure and the unit initial temperature, and we can set $\mathcal{L} = \mathcal{U}h = -h^3/[3\mu(1 - \mathcal{E})]$, $\mathcal{G} = 0$ and $\mathcal{C} = \pi^2(1 - \mathcal{E})/4h^2$. For the system of Wylie & Lister (1995), we let $\mathcal{E}$ represent the time-like variable they denote τ, $\mathcal{C} = 1/h$, $\mathcal{G} = 0$ and $\mathcal{L} = \mathcal{U} = -h^3/\bar{\mu}(\tau)$, where $\bar{\mu}(\tau)$ is an average viscosity defined by Wylie & Lister (1995) and which is determined from the along-channel evolution of the full, across-channel temperature profile, requiring prior numerical evaluation. We will refer to this latter approach as the 'unaveraged' system, since Wylie & Lister (1995) showed that it captures non-uniform steady states without approximation. Nonetheless, this system does involve an averaging over the channel and so is two-dimensional in space. As discussed by Wylie & Lister (1995), the equivalence between three-dimensional and two-dimensional steady states does not carry across to time-dependent states.

As shown in table 1, excluding the domain size, L_x, there are essentially four parameters: the dimensionless pressure drop, Π; the sensitivity of viscosity to temperature changes, γ; and the amplitude, A, and wavelength, λ, of the variations in the fissure width. As discussed by Wylie & Lister (1995), Π can be interpreted in a number of ways: as a dimensionless pressure drop; as a ratio of the thermal entry length to the length of the channel; or as the ratio of the characteristic rate at which heat is advected along the channel and the rate at which it is lost to the walls. Given our focus on the role of non-uniform fissure width, we largely take γ fixed, and consider Π, A and λ as our primary parameters. We first consider the uniform geometry ($A = 0$), in § 3.1, and identify the critical values of γ at which changes occur in the behaviour of steady-state solutions, as discussed by Helfrich (1995), Wylie & Lister (1995) and Morris (1996). The choice of $\gamma = 5.5$ is found to be sufficiently large that the system exhibits thermoviscous fingering and multiplicity of steady states, but not so large as to make the numerics intractable, since the numerical problem is found to become increasingly unstable with increasing γ. This value of γ corresponds to a viscosity ratio, $\mu_c/\mu_h = \exp(5.5)$, on the order of several hundred between the source temperature and the wall temperature, which is within the range of plausible values for the volcanic application. For example, Shaw (1969) suggests a value of $\beta = 0.1$ K^{-1} and Spera *et al.* (1982) also suggest a value between 0.02 K^{-1} and 0.1 K^{-1}. Taking these two values for β, we obtain a value of $\gamma = 5.5$ for temperature differences, $T_h - T_c$, of 275 °C and 55 °C, respectively.

To explore the impact of non-uniform geometry, we then vary λ between 0.2 and 20, and A between 0.01 and 0.1, solving for steady states of (2.22) over a wide range of pressure drops, Π, using the numerical method detailed in Appendix A. Table 2 gives the particular values (or ranges) of the parameters used to produce each figure. We evaluate the vertical flux through the fissure, $q_z(x, z) = 2\Pi\mathcal{L}\partial p/\partial z$, which provides the total flux per

Figure	Π	γ	A	λ	L_x
2	75–300	4.2–5.5	0	—	1
3(a,b)	230–285	5.5	0	—	10
3(c, d)	264	5.5	0	—	10
4	125–325	5.5	0.02–0.1	0.4–2	$\lambda/2$
5	200–300	5.5	0.01–0.1	0.2–20	$\lambda/2$
6	240	5.5	0.05	2, 1, 0.4	$\lambda/2$
7(a–c)	200–325	5.5	0.02	20	$\lambda/2$
7(d)	200–300	5.5	0–0.05	20	$\lambda/2$
8–9	200–235	5.5	0.02	2	$\lambda/2$
10	150–400	5.5	0.05 (random)	—	1
11	245	5.5	0.05 (random)	—	1
13	0–400	5.5	0	—	—
14	150–300	5.5	0.05	0.2–20	$\lambda/2$

Table 2. Values of dimensionless parameters used in each figure.

unit length of the fissure, $Q = (\int_0^{L_x} q_z \, dx)/L_x$, which is independent of z by conservation of mass. We also define the ratio of the maximum and minimum vertical fluxes at the surface,

$$Q_r \equiv \frac{Q_+}{Q_-} \equiv \frac{\max\limits_x q_z(x, z = 1)}{\min\limits_x q_z(x, z = 1)}, \tag{2.29}$$

which is a measure of degree of flow focussing. For comparison between sinusoidal geometries of different amplitudes, we scale this flux ratio by the value for the isothermal case (namely $(1 + A)^3/(1 - A)^3$), defining

$$\tilde{Q}_r \equiv \frac{(1 - A)^3}{(1 + A)^3} \frac{\max\limits_x q_z(x, z = 1)}{\min\limits_x q_z(x, z = 1)}. \tag{2.30}$$

We further evaluate the linear stability of the steady states to small perturbations. First, we revisit the uniform geometry, $A = 0$, and reproduce the main results of Helfrich (1995), Wylie & Lister (1995) and Morris (1996).

3. Results and analysis

3.1. *Uniform geometry*

Figure 2 shows the dimensionless flux per unit length, Q, as a function of the dimensionless pressure drop, Π, for planar (i.e. independent of x) steady-state solutions in the uniform geometry, $h = 1$, calculated using pseudo-arclength continuation. Here, we vary the value of the parameter governing the viscosity contrast, $\gamma = \log(\mu_c/\mu_h)$. In the following discussion, we report the quantitative results of the current model system, while a direct comparison to the corresponding values obtained from the models of Wylie & Lister (1995), Helfrich (1995) and Morris (1996) is given in Appendix B. The qualitative behaviour of the system is identical to that of the models in these previous studies. Namely, at low values of the viscosity contrast, the solution curve is single-valued and the planar steady states are stable. Above a first critical value, $\gamma_c = 4.8$, the curve becomes multivalued, resulting in three branches of the solution curve: a 'hot', fast branch at high pressure drops; a 'cold', slow branch at low pressure drops; and an intermediate branch
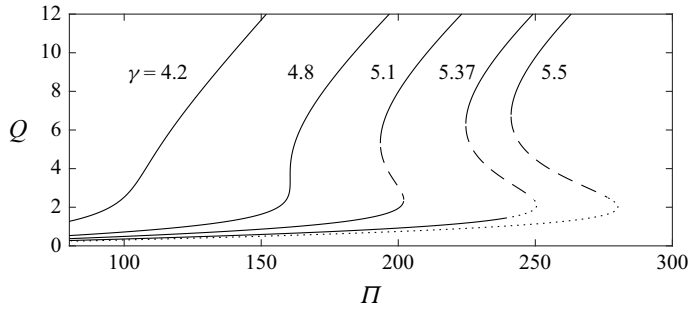
Figure 2. Dimensionless flux per unit length, Q, against dimensionless pressure drop, $\Pi \equiv \Delta p h_0^4 / \kappa \mu_h L^2$, for planar steady states in the uniform geometry, $h = 1$. Results are shown for several values of $\gamma = \log(\mu_c/\mu_h)$. The dimensional flux per metre is given by $\kappa L Q / h_0$. Solid lines show stable regions of the solution curve, and dashed and dotted lines show regions that are most unstable to planar and non-planar perturbations, respectively. See table 2 for other parameters used in these solutions.

on which the flux increases with decreasing pressure drop. As in previous studies, the intermediate branch is found to be unstable to a planar instability (i.e. to perturbations with vanishing wavenumber in the x-direction), which acts to drive solutions off the intermediate branch and towards the fast or slow branches of the solution curve. Above a second, higher, viscosity ratio, $\gamma_{3d} \approx 5.2$, there exist solutions which are most unstable to perturbations with non-vanishing wavenumber in the x-direction (see the dotted region of the solution curves for $\gamma = 5.37$ and $\gamma = 5.5$ in figure 2). This thus marks the onset of a fingering instability, analogous to classical Saffmann–Taylor viscous fingering, by which the uniform steady states go unstable to the formation of alternating regions of hot, low-viscosity fluid, and cold, high-viscosity fluid. At γ just above γ_{3d}, the region of the solution curve which is most unstable to the fingering instability is limited to a small region near the fold bifurcation that joins the slow and intermediate solution branches. As γ is increased further, this region extends down the slow solution branch and the entire slow branch becomes unstable to the fingering instability at a third critical value of the viscosity ratio, $\gamma_\infty \approx 5.4$. Thus, by $\gamma = 5.5$, the entire slow branch is unstable to the fingering instability and, as we will discuss later, we are able to find stable non-planar steady states reached after the onset of fingering. We report approximate values of γ_{3d} and γ_∞ here, because these results were calculated using our numerical method, with a finite domain ($L_x = 1$ in the cases shown in figure 2) and symmetry boundary conditions. This does not affect the calculation of Q for the planar steady states, nor the stability of the solutions to the planar instability; however, it does impact the stability to non-planar perturbations, since the finite domain restricts perturbations to those fitting inside the domain (with a half-integer number of wavelengths). Thus, for an infinite domain, γ_{3d} is likely slightly smaller than reported here. Similarly, the finite resolution of the grid sets a lower bound on the wavelengths that can be accurately captured. Since the wavelength of the most unstable mode decreases with decreasing Π (see later and Wylie & Lister 1995; Morris 1996), determining γ_∞ (where the fingering instability first extends to arbitrarily small values of Π) is difficult with our numerical method. Ultimately, our aim is to study the impact of a spatially varying channel width at a fixed value of γ and moderate values of Π (in the neighbourhood of the fold bifurcation), and not to accurately capture these critical values of γ for an infinite uniform geometry.

We now provide some more detail of the steady-state solutions for the uniform geometry, $h = 1$, and at $\gamma = 5.5$, fixed (now on a larger domain, $L_x = 10$). Figure 3(*a*) again shows the total flux per unit length of the fissure, Q, as a function of Π at steady state.
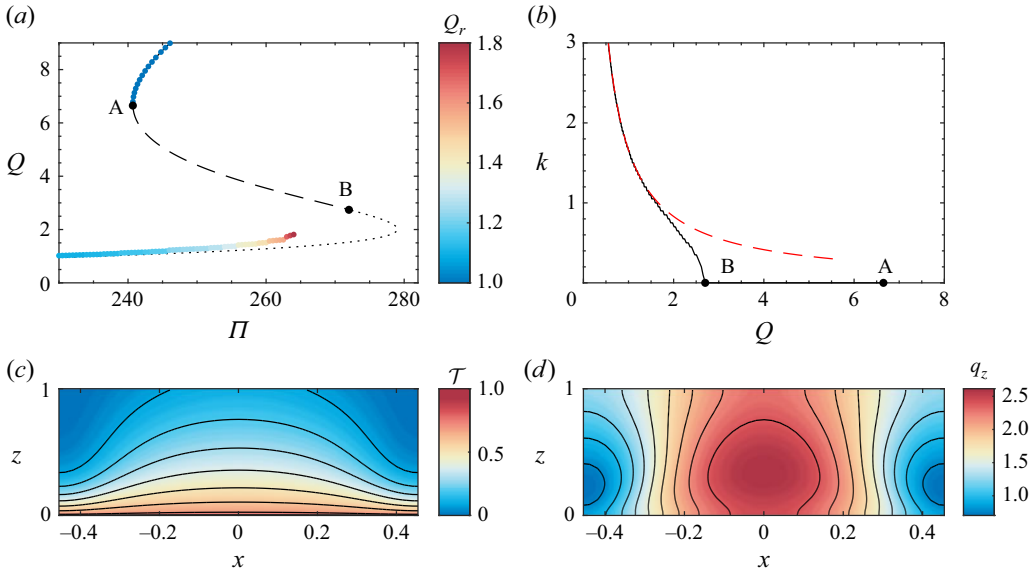
1015 A18-12

Figure 3. (*a*) Dimensionless flux per unit length of the fissure, Q, as a function of dimensionless pressure drop, Π, for stable steady states with $h = 1$ and $\gamma = 5.5$ (as in figure 2). The colour indicates the surface flux ratio, Q_r defined by (2.29), and the planar steady-state solution curve is shown by the black dashed and dotted line. Point A shows the fold bifurcation at which the solutions go unstable to planar perturbations, and point B indicates the location at which the solutions become most unstable to non-planar perturbations. (*b*) Wavenumber of the most unstable mode, k, as a function of Q (black). The red dashed line shows a curve proportional to $1/Q$. Points A and B as in panel (*a*). (*c*) Dimensionless cross-fissure average temperature, $\mathcal{T}$ defined in (2.13), for the last stable steady state near the slow branch at $\Pi = 264$. The domain has been reduced to show a single wavelength of the fingering pattern (of wavelength 0.909). The contours are plotted from $\mathcal{T} = 0.1$ near the top and increase in increments of 0.1. (*d*) Contour plot of vertical flux, $q_z = 2\Pi \mathcal{L} \partial p / \partial z$, for the solution shown in panel (*c*). The central (closed) contour is for $q_z = 2.4$, and values decrease in increments of 0.2 moving out from here. Note that the results in $x < 0$ have been produced by reflecting in $x = 0$ and have not been explicitly calculated. See table 2 for other parameters used in these solutions.

The black (solid, dashed and dotted) line shows the solution branch for the planar solutions (independent of x), as in figure 2. Point A indicates the fold bifurcation, below which the planar steady states are unstable. The wavenumber, k, of the most unstable mode for the unique planar steady state with flux, Q, is shown in figure 3(*b*). In panels (*a*) and (*b*), point B indicates the location at which the most unstable mode becomes non-planar ($k \neq 0$). Assuming the eruption starts at a high pressure drop and wanes with time, the structure of the bifurcation diagram gives the potential for the system to pass through the fold bifurcation and exhibit a sudden reduction in flux before localising due to the fingering instability. As reported by Wylie & Lister (1995) and Morris (1996), the wavenumber of the most unstable mode increases as Π decreases, and scales with $1/Q$ (see the red dashed curve in figure 3*b*) since the length scale is set by the thermal entry length. For our results, the wavenumber curve in figure 3(*b*) is stepped, which is simply the signature of the finite domain (in this case, $L_x = 10$) and symmetry boundary conditions, meaning that the wavenumers can only take half-integer multiples of $1/L_x$ – however, by taking the domain size to infinity, we could retrieve a perfectly continuous spectrum of wavenumbers.

Figure 3(*a*) also shows coloured points representing stable steady states. As noted previously, the fast branch of the planar solutions is stable. The stable solutions near the slow branch were obtained by natural continuation, starting at $\Pi = 200$ and increasing Π in steps of 0.5. At each step, the new steady state is either stable, in which case, it is kept;

or else, it is unstable, in which case, it is perturbed by its most unstable perturbation and evolved forwards in time until a new steady state is reached. The colour is set by the surface flux ratio, Q_r, defined by (2.29). Thus, $Q_r = 1$ on the fast, planar branch, and $Q_r > 1$ near the slow branch where there are flow-focussed regions. We found that at values of Π close to the onset of the non-planar instability (point B in figure 3), the perturbed solutions evolve onto the fast branch of the solution curve, resulting in no non-planar steady states, as was observed by Wylie & Lister (1995) when trying to find non-planar steady states. However, at lower Π, we find that the non-planar solutions evolve towards stable steady states with localised finger regions, as suggested by the solutions of Helfrich (1995). This result was also reproduced for the unaveraged system of Wylie & Lister (1995), but at a higher viscosity ratio, $\gamma = 6 > \gamma_\infty$, such that the entire slow branch is unstable to the fingering instability. The total flux of these flow-focussed states is slightly increased compared with the unstable steady state, and is distributed into higher and lower flux regions along the fissure. Among these solutions, the surface flux ratio and the wavelength of the finite amplitude fingering pattern both increase with Π, reaching a maximum surface flux ratio of $Q_r \approx 1.8$ at the last pressure drop before the non-planar solutions become unstable and instead evolve onto the fast branch (in this case, $\Pi = 264$). We again note that on this steady flow-focussed branch, the finite domain size and symmetry boundary conditions are relevant, since only a half-integer number of wavelengths can fit in the domain. Thus, the increase of the wavelength with increasing Π does not occur continuously, but in discrete jumps marked by a sequence of bifurcations. Indeed, since the solutions are calculated by natural continuation, figure 3(*a*) does not capture all stable steady-state branches; rather, there is a separate solution branch corresponding to each half-integer number of fingers within the domain, and the regions over which each branch is stable are overlapping. Thus, in figure 3(*a*), we follow a branch up to the Π at which it goes unstable, and then land on the next stable branch which is again captured up until the Π at which it goes unstable, and so on. The bifurcation which results in the onset of instability on one branch, and the transition to the next, is a subcritical pitchfork bifurcation (e.g. see Strogatz 2015*a*), involving the symmetry-breaking selection of which end of the domain switches from a hot to a cold finger (or *vice versa*). In contrast, for an infinite domain, $L_x = \infty$, we would anticipate that the flow-focussed steady-state branch would be a single continuous curve with a continually varying wavelength.

Figure 3(*c,d*) shows contour plots of the cross-channel average temperature, $\mathcal{T}$, and vertical flux, q_z, for the final stable steady solution on the non-planar steady-state curve at $\Pi = 264$, evidencing a finger structure with a wavenumber of $k = 1.1$ (i.e. 11 wavelengths in the domain of width $L_x = 10$), which is close to the most unstable wavenumber, $k = 1.2$, predicted for the uniform steady state at the same pressure drop. This figure also demonstrates why the ratio of fluxes at the surfaces, $Q_r = 1.8$, is not particularly large (compared with values obtained for the non-uniform geometry discussed later, see § 3.2), since the localisation occurs most significantly at depth before becoming more uniform nearer the surface where the magma is close to the wall temperature, $T = 0$. Under the model of a waning eruptive pressure drop (and assuming that the pressure drop varies sufficiently gradually that the system progresses through steady states), the system would drop off the fast branch at the fold bifurcaton around $\Pi = 240$ and first attain a non-planar solution at this value. In this case, the surface flux ratio would be smaller, resulting in a 14 % difference in flux between the hot and cold regions of the outflow. It should be noted that at $\gamma = 5.5$, we are not particularly far above the onset of the fingering instability (at $\gamma_{3d} \approx 5.2$), and one would anticipate that at larger viscosity ratios, the steady-state fingered solutions would exhibit a greater degree of flow-focussing. This will also be true

of the geometrically flow-focussed states, discussed in the following sections, and which we will show are associated with the fold instability arising first at $\gamma_c = 4.8$.

In this section, we have revisited the uniform geometry case, and shown that our results provide close qualitative agreement with the previous findings of Helfrich (1995), Wylie & Lister (1995) and Morris (1996), evidencing multiple steady states and the onset of the thermoviscous fingering instability at low pressure drops. Crucially, these results provide the baseline case against which to interpret the results in the non-uniform geometry, which we consider next. A quantitative comparison to the alternative averaging approaches of Helfrich (1995), Wylie & Lister (1995) and Morris (1996) is made in Appendix B, showing that the heat balance averaging of § 2.1 improves on the averaging of Helfrich (1995), but that there are nonetheless quantitative discrepancies with the unaveraged system. We note that there are multiple other approximations that are likely to have equally significant effects on the quantitative predictions of all models, in particular, the simple treatment of the thermodynamics at the fissure walls and the particular choice of the viscosity function, (2.5). For example, results of Wylie & Lister (1995, p. 248) employing a step-function model for the viscosity find a critical viscosity ratio, μ_c/μ_h, an order of magnitude smaller than when employing the exponential viscosity model (12 compared with 190), and Morris (1996, p. 126) finds a critical viscosity ratio of just 7.3 when the temperature of the fissure walls vary linearly with flow direction. In using the heat balance averaging detailed in § 2.1, we thus accept an additional source of approximation and associated quantitative discrepancy with the unaveraged system, in exchange for a number of advantages. As noted before, in employing the heat balance averaging, we consistently average the time derivative in the heat equation, meaning that time-dependent states (for example, those discussed in §§ 3.4 and 4) can be meaningfully considered alongside the steady states of the system – with both arising from the same assumed structure of the temperature profile and resulting average of the heat equation. Second, from a purely practical standpoint, in the unaveraged approach, evaluation of the functions $\mathcal{L}$ and $\mathcal{S}$, and their derivatives, relies on interpolation and numerical differentiation of a precomputed table of values, $\bar{\mu}(\tau)$. Furthermore, the derivative $d\mathcal{L}/d\tau$ diverges at $\tau = 0$. These features make the numerical solution of the resulting equations harder than when employing the analytical expressions for $\mathcal{L}$ and $\mathcal{S}$ arising from the heat balance averaging.

3.2. *Non-uniform geometry*

We now introduce a sinusoidal perturbation to the fissure width, at different amplitudes and wavelengths. Figure 4 shows the corresponding $Q(\Pi)$ steady-state solution curves for $\lambda = 0.4$, 1 and 2, and $A = 0.02$, 0.05 and 0.1. The solution curve corresponding to the planar solutions of the uniform geometry ($A = 0$) is shown as a dashed line and the colours now indicate the scaled surface flux ratio, $\tilde{Q}_r$ defined by (2.30). We also now use a logarithmic scale for the colour bar. We see that the effect of the non-uniform geometry is generally to replace the unstable intermediate branch of the planar solutions with a stable solution branch, exhibiting significant flux focussing. This stable, 'focussed', branch is either part of a continuous single-valued solution curve, or is connected to the original fast and/or slow branches by one or two pairs of fold bifurcations (for example, for $A = 0.05$ and $\lambda = 2$, there are two pairs of fold bifurcations, one at either end of the stable central branch). The deviation from the uniform geometry solution increases with both amplitude and wavelength. Further results for the scaled surface flux ratio, $\tilde{Q}_r$, are shown for a wider range of wavelengths and amplitudes in figure 5. For this plot, the solutions were found by natural continuation in the pressure drop, Π, starting on the fast branch with $\Pi = 400$ and integrating forwards in time to obtain stable steady states as Π is decreased
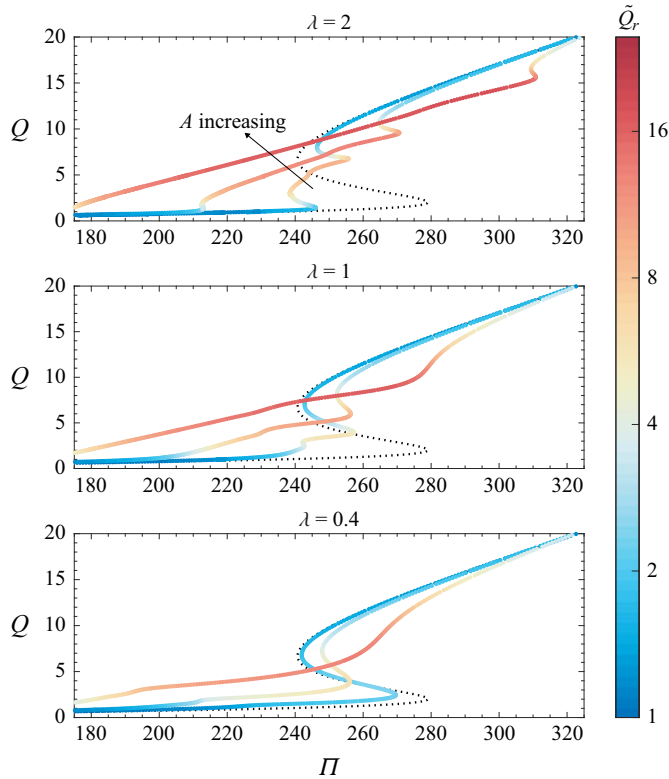
Figure 4. Steady-state solution curves for different amplitudes and wavelengths of the dimensionless fissure half-width, $h = 1 + A\cos(2\pi x/\lambda)$. Each panel shows average flux per unit length, Q, as a function of the dimensionless pressure drop, Π, as in figure 2, with points coloured by the scaled surface flux ratio, $\tilde{Q}_r$, defined by (2.30) (note the logarithmic colour scale). The wavelength, λ, is shown in the title and the three coloured curves correspond to amplitudes of $A = 0.02$, 0.05 and 0.1 (increasing in the direction shown). The solution curve for the planar steady states in the uniform geometry ($A = 0$) is shown as the black dotted curve in all panels. See table 2 for other parameters used in these solutions.
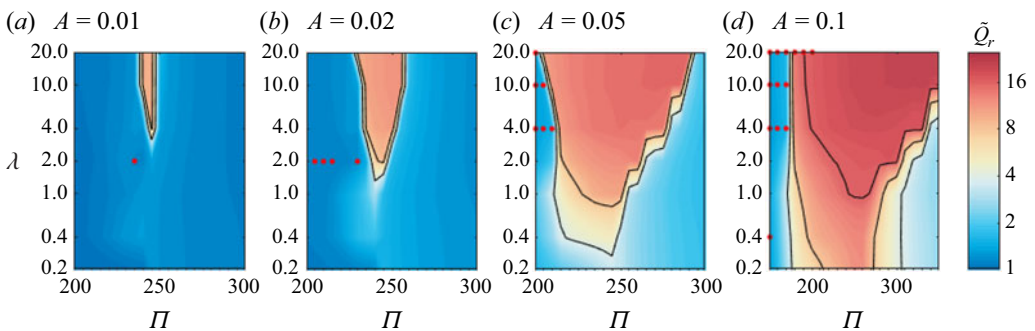

Figure 5. Colour plot of scaled surface flux ratio, $\tilde{Q}_r$ (2.30), as a function of dimensionless pressure drop, Π, and the wavelength of the variations in width, λ, at different values of the amplitude, A. Contours (black) are plotted at flux ratios of $\tilde{Q}_r = 4$ and 8 in all panels, and at the additional level $\tilde{Q}_r = 16$, in panel (*d*). The axis ticks indicate the location of solutions used to construct the contour plot, and red dots indicate that an average over the period of a periodic solution was used as opposed to a steady-state solution. Note the extended Π-axis in the final panel. See table 2 for other parameters used in these solutions.
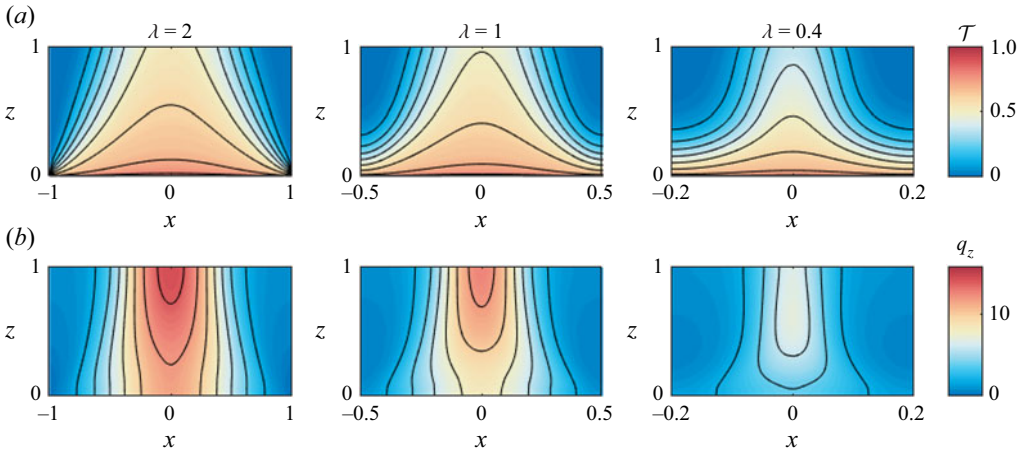
1015 A18-16

Figure 6. (*a*) Cross-channel average temperature, $\mathcal{T}$, defined in (2.13), for steady-state solutions at $\Pi = 240$ with $A = 0.05$ and $\lambda = 2$, 1, 0.4 (from left to right). The colour bar is shared between panels, and the contours are plotted from $\mathcal{T} = 0.1$ near the top left/right and increase in increments of 0.1. (*b*) Vertical flux, $q_z \equiv 2\mathcal{L}\partial p/\partial z$, for the same solutions. Contours are plotted from $q_z = 2$ at the left and right, and increase inwards in increments of 2. Note that the results in $x < 0$ have been produced by reflecting in $x = 0$, and have not been explicitly calculated. See table 2 for other parameters used in these solutions.

in discrete steps. This clearly evidences the existence of the highly localised solutions at intermediate pressure drops, and the dependence on the wavelength and amplitude of the fissure geometry. There are a small number of parameter values, primarily lying on the slow solution branch, at which no steady state was found (indicated by red dots in figure 5), and the solutions were instead found to be periodic. Oscillatory dynamics have previously been observed by Pailha *et al.* (2012) in experiments on isothermal fingers of air displacing viscous fluids, where geometrical constraints were found to play a key role (see also Thompson, Juel & Hazel 2014; Franco-Gómez *et al.* 2016; Lawless, Hazel & Juel 2024). The structure of the periodic solutions observed in these cases is rather different from those observed here. We explore the periodic solutions in more detail in § 3.4, but note that since these have a period-averaged surface flux ratio in line with neighbouring steady solutions (see figure 5), the implication for the degree of fissure localisation is minimal. The temperature and flux distributions are shown in figure 6 for steady-state solutions at $\Pi = 240$ on the focussed branch for $A = 0.05$ and $\lambda = 2$, 1 and 0.5. These can be compared with figure 3(*d*,*e*) for the focussed solutions arising from thermoviscous fingering in a uniform geometry at $\Pi = 264$, showing that the temperature variations penetrate further up the fissure and that the vertical flux variations are several times larger.

The physical origin of the stable, highly localised branch can be readily understood as the wider region of the fissure remaining in the hot, fast flowing state, while the thinner region transitions to the cold, slow state as the pressure drop decreases. The flow in the wider region is cognate with the fast branch of the planar solution, and the flow in the narrower region is cognate with the slow branch of the planar solution. Thus, the occurrence of geometrical focussing is more closely associated with the fold bifurcation and planar instability exhibited by the uniform-width system than it is with the thermoviscous fingering instability. The dependence on amplitude and wavelength can also be easily explained. Naturally, a larger amplitude results in a greater difference in flow rate and hence heat advection through the different regions of the fissure. However, if the wavelength is small, then the hot and cold regions can exchange heat more easily, resulting in a more uniform temperature and a reduction in the geometric effect. Note that

this exchange of heat does not occur diffusively, since the reduced heat equation includes no diffusion in the plane of the fissure (see (2.9)); rather, it occurs through advection due to along-fissure pressure gradients. These pressure gradients are stronger when the length scale between the regions of the fissure are smaller, and thus the solutions become more uniform for smaller λ (e.g. compare solutions for $\lambda = 2$ and $\lambda = 0.4$ in figure 6). Another way to understand the suppression of geometrical localisation at short geometrical wavelength is by reference to the fingering instability in the uniform geometry. Here, Wylie & Lister (1995) and Morris (1996) showed that the preferred wavelength of the fingering instability is comparable to, or larger than, the thermal entry length, which scales with Q. The geometrical localisation occurs via the above mentioned mechanism at values of Π near the location of the fold bifurcations associated with multiplicity of steady states in the planar problem (see figure 4), and hence at solutions which have fluxes of the order $1 \lesssim Q \lesssim 10$. Therefore, by analogy with the result for the uniform geometry, for geometrical wavelengths significantly smaller than these $O(1)$ thermal entry lengths, the localisation into features on the length scale of the topography is suppressed.

3.3. *Long-wavelength regime*

In the regime of long wavelength, $\lambda \gg 1$, the different regions of the fissure are unable to 'communicate' with one another and a leading order analysis can be undertaken in which x-derivatives vanish, and every vertical slice of the fissure can be considered as a planar problem of a different thickness. This regime is an interesting end member and could represent the variation of fissure width on the length scale set by the full length of the fissure – typically fissures are widest at their centres and get increasingly thin towards their ends. When the wavelength of the perturbation to the width is long, we can rescale the x-coordinate by λ and consider the variables to be asymptotic series in $1/\lambda \ll 1$. Taking only the leading order of the governing equations, we obtain

$$\frac{\partial \mathcal{E}}{\partial t} + \Pi \frac{\partial}{\partial z}\left(\mathcal{S}(\mathcal{E})\frac{\partial p}{\partial z}\right) = \frac{2\Theta}{\delta}, \quad \frac{\partial}{\partial z}\left(\mathcal{L}(\mathcal{E})\frac{\partial p}{\partial z}\right) = 0. \tag{3.1}$$

Namely, the equations for the planar problem, with x entering only as a parameter via the width, $h(x)$. These equations and the resulting steady-state flux, Q, can then be rescaled to the case with $h = 1$, by writing

$$\mathcal{E} = h\tilde{\mathcal{E}}, \quad \delta = h\tilde{\delta}, \quad \mathcal{S} = h^3\tilde{\mathcal{S}}, \quad \mathcal{L} = h^3\tilde{\mathcal{L}}, \quad \Pi = \tilde{\Pi}/h^4, \quad t = h^2\tilde{t}, \text{ and } Q = \tilde{Q}/h. \tag{3.2}$$

Thus, given the uniform steady-state solution curve (Π_0, Q_0), we can find a steady-state solution curve for the position x in the non-uniform fissure, as $(\Pi_0/h^4, Q_0/h)$. In particular, at the widest region, we have $h = 1 + A$ and at the thinnest region, we have $h = 1 - A$. Figure 7(a) shows the result of this rescaling for $A = 0.02$: the wider geometry (dashed) exhibits a higher flux and consequently transitions from the fast branch to the slow branch via a pair of fold bifurcations at a lower pressure drop; conversely, the narrower geometry (dotted) exhibits a lower flux and transitions between the branches at a higher pressure drop. If we then consider the average of the fluxes at each pressure drop, we obtain a new curve shown by the solid curve. The curve in figure 7(b) shows the prediction for the ratio of fluxes, $Q_r \equiv Q_+/Q_-$, in the wider and thinner regions of the fissure, from this long-wavelength analysis. From these two panels, we observe that the solution curve exhibits the key features of the non-uniform geometries at larger wavelengths, namely a stable middle branch with significant flux localisation (large Q_r), connected to the fast and slow branches by two pairs of fold bifurcations. Also shown as points in each panel are the results of numerical solutions for $A = 0.02$ and $\lambda = 20$. These were obtained by natural
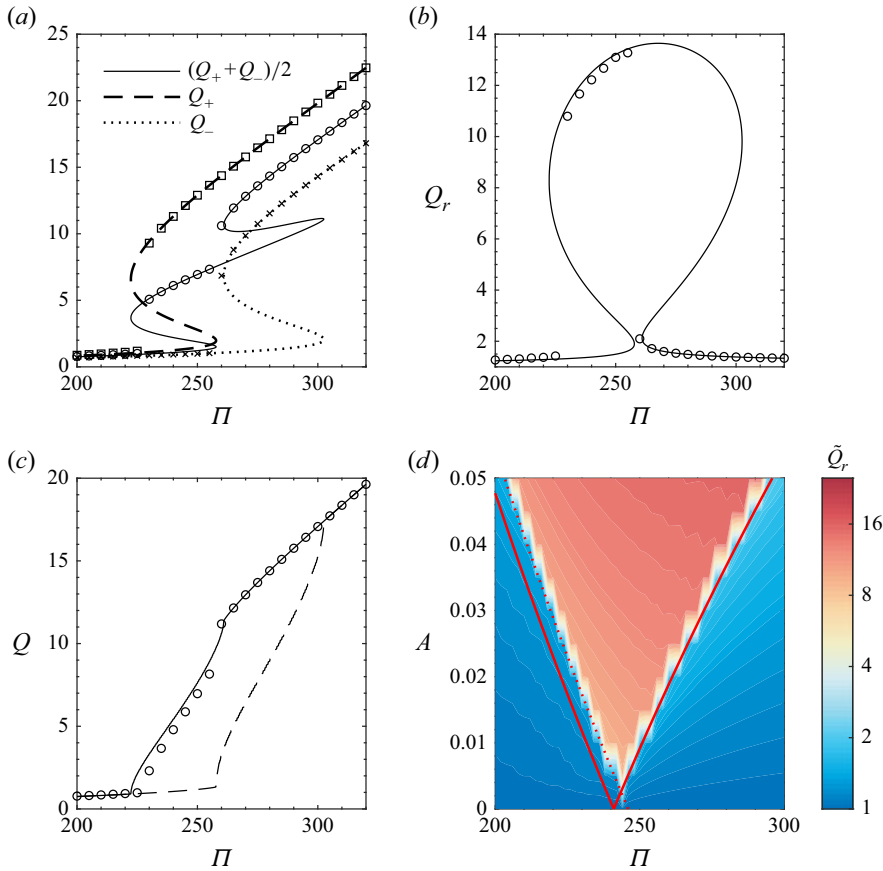
Figure 7. (*a*) Steady-state solution curve (as in figure 3) for the uniform geometry, $h = 1$, re-scaled to the width of the widest, $h = 1 + A$ (black dashed), and thinnest, $h = 1 - A$ (black dotted), regions of the non-uniform geometry with $A = 0.02$ and $\lambda \to \infty$ according to (3.2). These represent the maximum, Q_+, and minimum, Q_-, surface fluxes in the non-uniform geometry. The black solid curve shows the average of the fluxes, $(Q_+ + Q_-)/2$. Points are shown from numerical solutions with $A = 0.02$ and $\lambda = 20$, obtained by natural parameter continuation in decreasing Π (Q_+, squares; Q_-, crosses; average, circles). (*b*) Ratio of maximum and minimum flux, $Q_r = Q_+/Q_-$, as a function of Π. The line is obtained from taking the ratio of the fluxes represented by the dashed and dotted lines in panel (*a*), and the circles are obtained from the numerical simulations, as in panel (*a*). (*c*) Average flux per unit length, Q, as a function of Π. The lines are obtained by the long wavelength approximation (3.4). The different curves correspond to continuation in Π in either the decreasing (solid) or increasing (dashed) directions. Also shown as circles are the numerical results as in panels (*a*) and (*b*). (*d*) Colour plot of scaled surface flux ratio, $\tilde{Q}_r$ (defined by (2.29)), as a function of Π and A for numerical solutions with $\lambda = 20$. The solid red lines show the boundaries predicted by the long-wavelength analysis ($\Pi = 241/(1 + A)^4$ and $\Pi = 241/(1 - A)^4$), and the red dotted line shows the predicted lower boundary offset by a pressure drop of 5. Note the logarithmic colour scale. See table 2 for other parameters used in these solutions.

continuation in decreasing Π, so the whole solution curve is not obtained; however, the branches that are obtained match the predictions well, closely capturing the maximum and minimum fluxes, Q_+ and Q_-, and their ratio, Q_r, and showing roughly the same critical pressure drops where the solutions change from one branch to another.

We note that the use of the average of the largest and smallest fluxes, $(Q_+ + Q_-)/2$, in figure 7(*a*) is not the same as the average flux per unit length, Q, used previously, but was chosen here for illustrative purposes. To obtain the prediction for Q, we must account

for the continuous variation of the width, h. Suppose we have the flux as a function of the pressure drop, $Q_0(\Pi_0)$, from the uniform geometry results (the choices made in defining such a function are discussed later). To obtain a long wavelength prediction for the average flux per unit length of the non-uniform geometry, we can then calculate

$$Q(\Pi) \approx \frac{1}{L_x} \int_0^{L_x} \frac{Q_0(h(x)^4 \Pi)}{h(x)} \, \mathrm{d}x, \tag{3.3}$$

which, for the sinusoidal width, $h = 1 + A \cos(2\pi x / \lambda)$, is independent of wavelength

$$Q(\Pi) \approx \frac{2}{\lambda} \int_0^{\lambda/2} \frac{Q_0(h^4 \Pi)}{h} \, \mathrm{d}x = \frac{1}{\pi} \int_{1-A}^{1+A} \frac{Q_0(h^4 \Pi)}{h \sqrt{A^2 - (1-h)^2}} \, \mathrm{d}h. \tag{3.4}$$

We note that the solution curve (Π_0, Q_0) does not immediately provide a well-defined function $Q_0(\Pi_0)$, due to the multiplicity of steady states. There is, however, a natural choice by which to define two such functions, corresponding to natural parameter continuation in either decreasing or increasing Π. For the former, wherever $Q_0(\Pi_0)$ is multivalued, we choose to take Q_0 from the fast, hot branch, while in the latter, we instead evaluate the flux from the slow, cold branch. The resulting predictions for the average flux, Q, for the sinusoidal geometry with $A = 0.02$ are shown in figure 7(*c*). Here, the solid line is for the natural continuation in decreasing Π and is compared against the fluxes obtained from the numerical solutions with $\lambda = 20$ (circles, also obtained by continuation in decreasing Π). These show good agreement. The dashed line, for comparison, shows the prediction for natural continuation in increasing Π, giving a lower flux where the two differ.

For the current parameters and the uniform geometry, $h = 1$, the fold bifurcation on the fast branch occurs at $\Pi \approx 241$ at which the flux drops from $Q \approx 6.6$ to $Q \approx 1$ (when continuing naturally in decreasing Π). Thus, for the long-wavelength approximation, we anticipate the first fold bifurcation to occur at $\Pi = 241/(1 - A)^4$. At this bifurcation, the thinner region exhibits a reduction in flux by a factor of $6.6/(1 - A)$, while the wider region maintains the same flux. Thus, the surface flux ratio increases by a factor of $6.6/(1 - A)$ when the solution drops onto the focussed branch at this point. The second fold bifurcation is predicted to occur at $\Pi = 241/(1 + A)^4$, where the surface flux ratio decreases by a factor of $6.6/(1 + A)$. Thus, as the amplitude, A, decreases towards zero, the stable focussed branch shortens but persists, ultimately shrinking to the point $\Pi = 241$, with $Q_+ = 6.6$ and $Q_- = 1$, as $A \to 0$. The prediction for the critical values of Π which bound the focussed branch is compared with numerical solutions for $\lambda = 20$ in figure 7(*c*) showing good agreement for the upper boundary, $\Pi = 241/(1 - A)^4$, but weaker agreement for the lower boundary where the long-wavelength analysis under-predicts the critical pressure drops observed in the numerical solutions by roughly 5 at all amplitudes (this is also noticeable in the other panels of figure 7 for the specific choice of $A = 0.02$). It is unclear what causes this discrepancy. However, since the thinner region lies on the slow branch of the solution curve, it becomes unstable to the thermoviscous fingering instability, resulting in finger structures within the cool, slow region of the fissure. The wavelength of these fingers decreases with decreasing pressure drop, Π, and so it is possible that the assumption of large length scale in the x-direction becomes invalid at the boundary between the hot and cold regions as the critical pressure drop is approached. In general, if gradients are greater in the x-direction than implied by the rough scaling, $1/\lambda \ll 1$, this will promote heat fluxes between the regions, resulting in a transition to the uniformly slow branch at larger Π. Nonetheless, the predictions of the long-wavelength analysis give a decent agreement to the numerical solutions, particularly
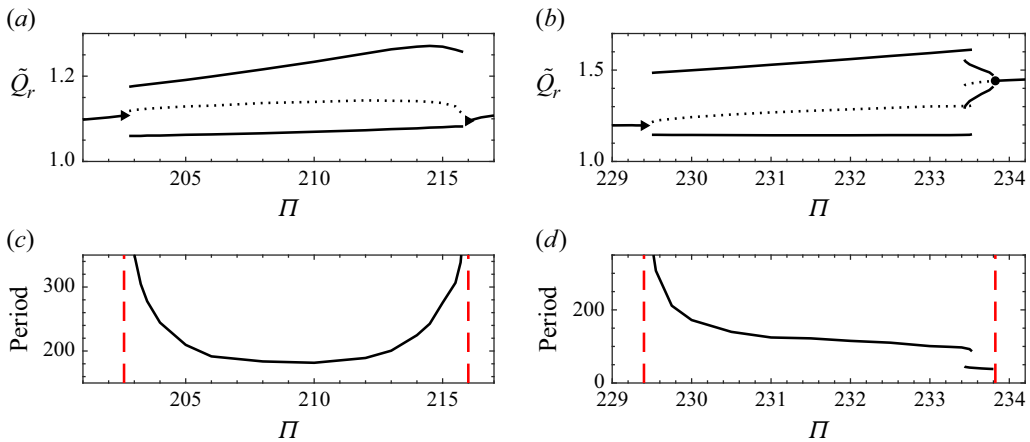
1015 A18-20

Figure 8. (*a,b*) Scaled surface flux ratios, $\tilde{Q}_r$, as a function of the dimensionless pressure drop, Π, for steady and periodic solutions with $A = 0.02$ and $\lambda = 2$ over two ranges of Π corresponding to the absence of stable steady states in figure 5(*b*). For periodic solutions, the maximum and minimum values of $\tilde{Q}_r$ are plotted as solid lines, and the average over the period is plotted as a dotted line. Markers indicate the bifurcations at which the steady branches lose stability, with triangles corresponding to infinite period bifurcations and the dot indicating a supercritical Hopf bifurcation. (*c,d*) Period of the solutions as a function of Π, with the two panels corresponding to the branches shown in panel (*a,b*). Red dashed lines indicate the ends of the stable steady-state solution branches at either side. See table 2 for other parameters used in these solutions.

for the critical pressure drop resulting in the onset of localisation, which is perhaps of greatest concern for the volcanological application.

3.4. *Periodic solutions*

Here, we detail the origin and the bifurcation structure of the periodic solutions evidenced by the absence of steady states at points marked in red in figure 5(*b*). We take two examples of branches of periodic solutions along the solution curve for $A = 0.02$ and $\lambda = 2$, tracking the solutions as Π is varied. For these solutions, we took $L_x = 1$, i.e. the smallest domain that captures the $\lambda = 2$ wavelength, given the symmetry boundary conditions at either end. The scaled surface flux ratio, $\tilde{Q}_r$, and the period are plotted as functions of Π in figure 8, showing that one periodic solution branch persists over the range $202.6 \lesssim \Pi \lesssim 216$ and two different periodic branches occur over the range $229.4 \lesssim \Pi \lesssim 233.8$. At $\Pi \approx 233.8$, on the steady solution branch, a pair of complex eigenvalues of the stability problem cross the imaginary axis, indicating a Hopf bifurcation. The amplitude of the stable periodic solutions obtained near $\Pi = 233.8$ grows from zero, and their period starts at that of the unstable periodic mode at the bifurcation, $2\pi/\text{Im}(\sigma) \approx 38$. Thus, the bifurcation to the periodic solution is a supercritical Hopf bifurcation (e.g. see Strogatz 2015*b*). The periodic solution branch arising at the Hopf bifurcation is short-lived, becoming unstable to a fold bifurcation at $\Pi \approx 233.45$, resulting in the system transitioning to a new stable periodic solution branch, with a longer period and larger amplitude. At the other end of this periodic solution branch, the periodic solution is destroyed in an infinite period bifurcation at $\Pi \approx 229.4$, where a saddle-node point appears on the periodic orbit and the system follows the new stable steady-state solution branch at lower Π. The period-averaged scaled surface flux ratio, $\tilde{Q}_r$, is naturally continuous at this bifurcation, since the periodic solution spends an increasing proportion of its (diverging) period close to the state that becomes the stable steady solution after the bifurcation. For the second periodic solution branch, shown in figure 8(*a,c*), the bifurcation structure is slightly different, with the transition between the

1015 A18-21

steady-state and periodic solution branch resulting from an infinite period bifurcation at both ends.

Figure 9 shows the dimensionless average temperature, $\mathcal{T}(x, z)$ (see (2.13)), for a selection of solutions along the same solution branch (i.e. for the sinusoidal geometry with $A = 0.02$ and $\lambda = 2$). Panels (a)–(c) show steady solutions at $\Pi = 200, 220$ and 234, representing solutions on the three steady-state branches separated by the periodic solution branches in figure 8. These indicate how the spatial structure of the fingered states changes after passing through the periodic solution branches. The other panels show three states obtained at particular times (with $t = 0$ chosen arbitrarily) during the periodic solutions at $\Pi = 210$ (panels d–f) and $\Pi = 232$ (panels g–i), indicating that these solutions exhibit oscillations between states that are similar in structure to stable steady solutions at larger and smaller values of Π. While the exact details of two fingered solutions might vary subtly, there are two main factors that govern the broad configuration of a solution. The first is the number of fingers in the domain or, equivalently, the average wavelength of the fingers. The second is the location of these fingers, which (given the symmetry boundary conditions) largely corresponds to a binary choice of whether $x = 0$ corresponds to a (relatively) hot or cold region of the fissure. As for the uniform case (see figure 3b), the preferred wavelength of fingers scales with the thermal entry length and, thus, the average wavelength increases as Π increases. For example, at $\Pi = 200$ (figure 9a), the solution exhibits five hot fingers per wavelength of the fissure geometry (half of this wavelength, $\lambda = 2$, is shown in each panel), while at $\Pi = 220$ and $\Pi = 234$ (figure 9b,c), there are four. In the non-uniform geometry, the preferred wavelength also depends on the local width of the channel, with longer wavelengths preferred in wider regions (since the thermal entry length also increases with channel width). This effect is visible in figure 9, where the wavelength of the fingering pattern generally gets shorter between the widest region of the channel, at $x = 0$, and the narrowest, at $x = 1$. The dependence on Π of the choice between a hot or cold region at $x = 0$ is less clear. Naively, one might anticipate that the most stable configuration would be one in which the widest point of the channel is hot and/or the narrowest point is cold. However, given the continuous variation of fissure width, the situation turns out to be more subtle than this. For example, at $\Pi = 200$, both choices result in stable steady states. Similarly, both configurations arise during the periodic solution at $\Pi = 210$ (see figure 9e,f). In figure 9(a), we show the state with a cold region at $x = 0$, which is the solution reached when continuing in Π from the periodic solution branch at $202.6 \lesssim \Pi \lesssim 216$ (i.e. it is a state similar to that shown in figure 9(f), and not panel (e), that becomes the saddle-node point in the infinite period bifurcation at $\Pi \approx 202.6$). This is also the configuration which is the more stable of the two at $\Pi = 200$ (in the sense that the growth rate of its least stable mode is more negative). In general, the preferred configuration depends on Π. For example, both the solutions at $\Pi = 220$ and $\Pi = 234$ in figure 9(b,c) have an average wavelength of 0.5, but the solutions have opposite configurations. There are thus several (potentially) competing influences on the configuration of fingers in a flow-focussed state: the preferred wavelength of fingers in an average sense; the preferred wavelength of fingers locally, due to the local channel width; and the relative stability of the two choices of finger location. The periodic solution branches then arise where these influences are in conflict and no choice of configuration is stable, with the solution instead oscillating between multiple, weakly unstable states. During a periodic orbit, the evolution between these states happens in two main ways: a propagation of the fingers down the length of the fissure (e.g. panels e,f and g,i in figure 9); or the removal or addition of a finger at one or both ends of the domain (e.g. the evolution to and from panels d and h). As demonstrated in figure 8, the periodic solution branches can evidence a range of different behaviours, and we do not claim to have provided
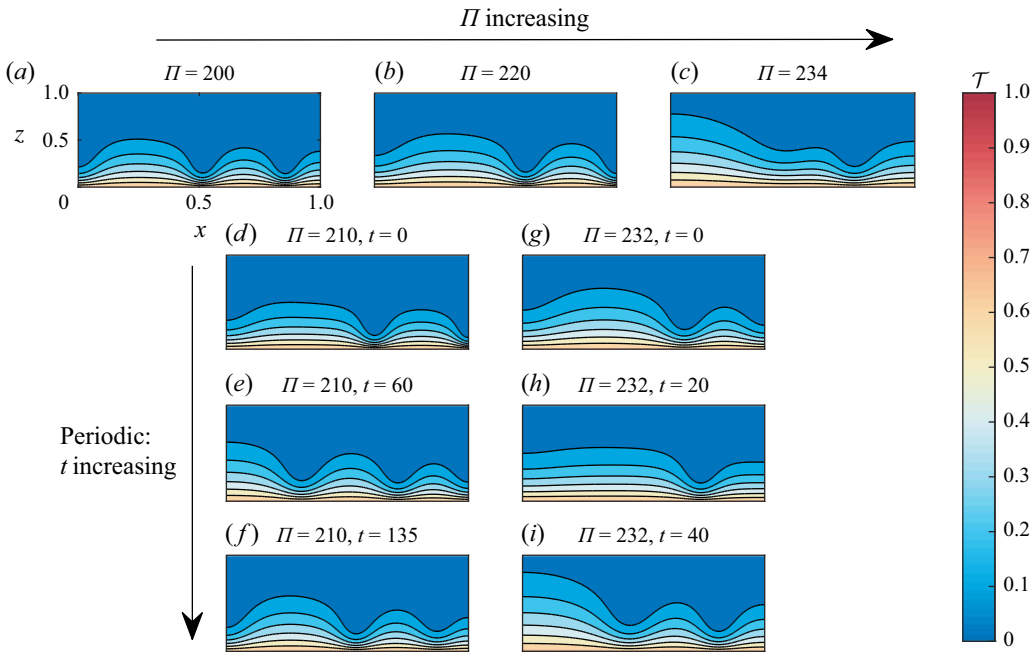
Figure 9. Colour plots and contours of average temperature, $\mathcal{T}$, for several solutions in the sinusoidal geometry with $A = 0.02$ and $\lambda = 2$. (*a–c*) Steady solutions at (*a*) $\Pi = 200$, (*b*) $\Pi = 220$ and (*c*) $\Pi = 234$. Panels (*d*)–(*f*) and (*g*)–(*i*) show snapshots at several times in the periodic solutions at $\Pi = 210$ (period ≈ 182) and $\Pi = 232$ (period ≈ 115), as indicated in the titles, and $t = 0$ chosen without loss of generality. Contours are plotted from $\mathcal{T} = 0.1$ nearest the top of each panel, increasing in increments of $\mathcal{T} = 0.1$. The axes are the same in all panels, and are omitted from all but panel (*a*) to avoid crowding. See table 2 for other parameters used in these solutions.

an exhaustive exploration of these states. We also note that no periodic solutions were observed for the uniform geometry. Two of the factors previously discussed (the spatially varying preferred wavelength, and the choice for the location of the hot and cold fingers) are absent without the presence of wider and narrower regions of the fissure, and so it is perhaps unsurprising that the uniform geometry does not exhibit oscillatory dynamics.

4. Discussion and implications

The results in §3 indicate that geometric localisation in a dyke with sinusoidally varying width tends to overprint localisation via the thermoviscous fingering instability observed in planar dykes. It also leads to a greater degree of localisation under similar conditions: the magnitude of the surface flux ratio on the focussed branch takes substantially larger values (in the range $2-16$ for the results shown in figure 4) than those obtained for the steady state that arises through viscous fingering (see figure 3). Furthermore, the localisation occurs at higher pressure drops, before the entire system lies on the cold, slow branch. A 5 % non-uniformity, $A = 0.05$, is fairly modest compared with the variations seen in volcanic fissures (Parcheta *et al.* 2015), and figures 4 and 5 indicate that above this amplitude, there are large regions of the parameter space where there is significant localisation through geometric effects, particularly at large wavelengths. While many of the irregularities observed in natural systems have relatively short wavelengths (Parcheta *et al.* 2015), at the very least, fissures are typically wider at their centre and taper towards their ends (Daniels *et al.* 2012). The model we present does not extend to a fissure which is

completely closed at its ends, but the full length of the fissure does set a large wavelength variation in fissure width. It therefore seems very plausible that the localisation of these natural systems is dominated by the non-uniformity of the geometry, rather than the spontaneous localisation driven by viscous fingering.

In practice, fissure geometries are not strictly sinusoidal, and natural variability is likely better represented by a random superposition of a range of wavelengths and amplitudes. While the nonlinearity of the system means that solutions cannot be formed simply by superposition of the solutions for the sinusoidal geometries, we nonetheless anticipate that the qualitative results regarding the occurrence of geometry-dominated flow focussing will carry across to such geometries. Rather than explore a wide range of different randomised geometries, here we give one example of the implications of the above mentioned conclusions for such a geometry. Fault and fracture geometries are often modelled by a power-law roughness, $P(\lambda) \propto \lambda^{\alpha}$, where $P(\lambda)$ is the power spectral density of the mode with wavelength λ and α is a constant typically between 2 and 3 (Méheust & Schmittbuhl 2000; Auradou *et al.* 2005; Candela *et al.* 2012; Brodsky *et al.* 2016). The geometry we consider has been generated with $L_x = 1$ and $\alpha = 2.2$ (the value reported by Brodsky *et al.* (2016) for the geometry of fault surfaces), and we cut off the power-spectrum below a wavelength of $\lambda = 0.01$, which would be poorly resolved at the resolution of the discrete grid. We further scale the values of h such that $0.95 \leqslant h \leqslant 1.05$, corresponding to $A = 0.05$ in the case of the sinusoidal non-uniformity. The resulting randomised geometry is shown in the inset of figure 10(*a*). We then calculate steady and unsteady states of the system at different dimensionless pressure drops, Π, using the same numerical method as for the sinusoidal cases.

Figure 10(*a*) shows the surface flux, $q_z(x, z = 1)$, scaled by the total flux per unit length of the fissure, Q. As anticipated from the results for the sinusoidal case, when the pressure drop is sufficiently large or sufficiently small, the variation in the surface flux is fairly minor and is dictated primarily by the $h(x)^3$ factor for an isothermal fluid. In contrast, when the pressure drop takes intermediate values, $200 \lesssim \Pi \lesssim 300$, the system localises strongly at the positions of maximal width, due to the interaction between the geometry and the thermoviscosity. The region of Π and the magnitude of the flux ratio is consistent with the results for $A = 0.05$ in the sinusoidal case (see figures 4 and 5*c*). Figure 10(*b*) shows the steady-state solution branch, with colours indicating the degree of flux localisation. Whereas the sinusoidal fissure geometries exhibit a single focussed branch, the solution curve for the randomised geometry suggests two successive stages of localisation. On decreasing the pressure drop, the system first transitions to a focussed state in which the left side of the fissure reduces in flux significantly, but three wider sections of the fissure remain at high flux states (see $\Pi = 245$ in figure 10*a*). A second transition occurs before $\Pi = 235$, where the thinner of these three sections enters the slow regime, leaving the fissure localised in the central region (see $\Pi = 235$ in figure 10*a*). Finally, the system transitions to the slow branch at $\Pi \approx 225$, although the fissure remains fairly localised at the single widest point, where the flux gradually weakens as the pressure drop is decreased. The flux is largely uniform again by $\Pi = 150$. These transitions are further shown in figure 10(*c*), which plots the surface flux, q_z, scaled by both the total flux per unit length of fissure, Q, and the isothermal factor, h^3. The localised branches are evidenced by regions of varying colour along slices of constant Π.

It is informative to consider the dimensional quantities for plausible volcanological parameters. As an illustrative example, we consider parameter values appropriate for a typical Hawaiian fissure eruption, as given in § 2. In this case, the flux scale is $\kappa L/h_0 \approx 0.002$ m^3 s^{-1} per metre length of the fissure. Thus, for the ranges of dimensionless flux per unit length, Q, reported here, a kilometre of fissure would have a volume flux between
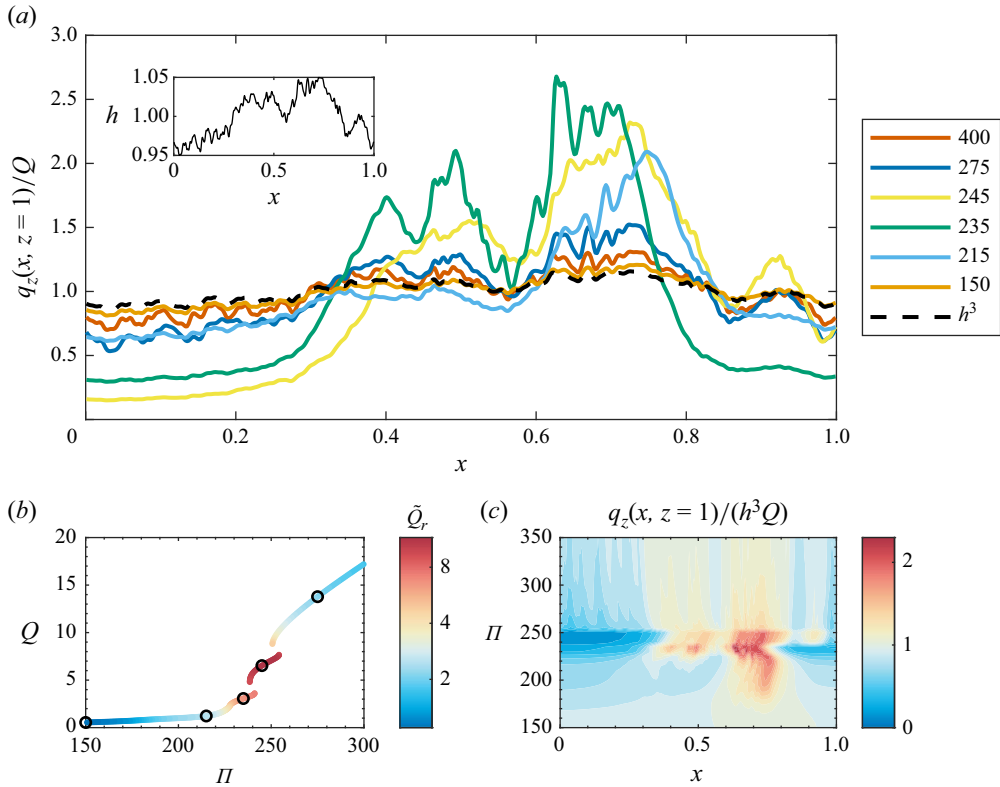
Figure 10. (*a*) Scaled vertical flux at the surface, $q_z(x, z = 1)/Q$, as a function of position, x, for the randomised geometry, $h(x)$, shown in the inset. The different coloured lines correspond to different dimensionless pressure drops, Π (see legend). The black dashed line shows the isothermal factor, h^3. (*b*) Steady-state solution curve for the randomised fissure geometry. Coloured points are stable solutions coloured according to the scaled surface flux ratio, $\tilde{Q}_r$ ((2.30) with $A = 0.05$), and black circles indicate the solutions shown in panel (*a*), excluding $\Pi = 400$ which is off the scale. (*c*) Colour plot of surface flux, $q_z(x, z = 1)$, scaled by $h^3 Q$, as a function of position, x, and pressure drop, Π. See table 2 for other parameters used in these solutions.

2 and 40 m^3 s^{-1}, with the localisation occuring when the flux drops below approximately 20 m^3 s^{-1}. This range of fluxes is consistent with estimates from fissure eruptions in Hawaii (Tilling *et al.* 1987). It is also of interest to obtain some measure of the time scale on which the system evolves. Figure 11 shows one example of a time-dependent solution for the randomised fissure geometry shown in the inset of figure 10(*a*). In this case, the system was initiated with $\Pi = 245$ and with a temperature distribution close to the inlet temperature, $T = 1$, throughout the fissure (specifically, $\mathcal{E}/h = 0.01 \implies \mathcal{T} = 0.99$ everywhere). The system then evolves towards the steady state, which lies on one of the flow-focussed branches of the solution curve. As shown in figure 11, this relaxation to the new steady state occurs of the order of 2 dimensionless time units (becoming very close for $t \gtrsim 4$). This is also in line with the time scale implied by the decay rate of the least stable perturbation to the steady state, given by $-1/\max(\mathrm{Re}(\sigma)) = 1.3$. With the dimensional parameters for a typical Hawaiian fissure eruption given in § 2, the time scale, h_0^2/κ, is of the order of a day or two, and thus the adjustment shown in figure 11 would occur over the course of a few days. This is comparable to, although perhaps on the longer end of, the time scales for localisation observed in fissure eruptions (Richter *et al.* 1970;
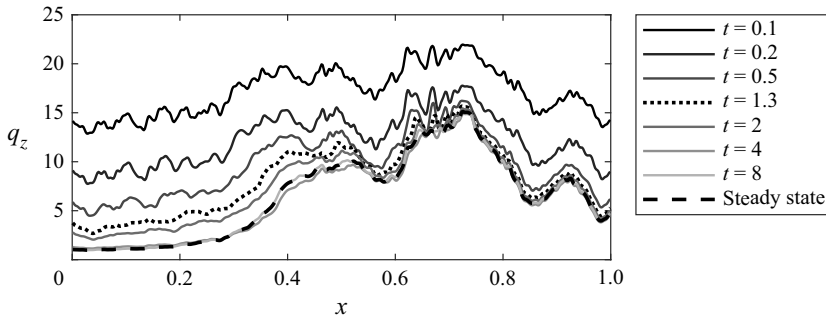
Figure 11. Evolution of surface flux, $q_z(x, z = 1)$, for the randomised fissure geometry when initiated at $t = 0$ from a uniformly hot state, $\mathcal{E}/h = 0.01$, with $\Pi = 245$. The steady-state solution for $\Pi = 245$ is indicated by the dashed black line, while the dotted line corresponds to the time scale implied by the slowest decay rate of linear perturbations to the steady state, $t = -1/\max(\mathrm{Re}(\sigma)) \approx 1.3$. See table 2 for other parameters used in these solutions.

Thorarinsson *et al.* 1973; Eibl *et al.* 2017). Additional physical effects, not incorporated into this model and discussed later, are likely to enhance localisation and thus shorten the time scale on which it occurs. Finally, we note that the typical dimensionless pressure drop, $\Pi = 260$, estimated for a dimensional pressure drop of 10^7 Pa, is within the range where the geometrically flow-focussed solutions are typically found ($200 \lesssim \Pi \lesssim 300$, see figures 4 and 10), and so it is plausible that this is a significant factor in the localisation of fissure eruptions.

This work predominantly employed a width-averaged model, while retaining the essential structure of the cross-channel temperature profile, to efficiently capture the key qualitative behaviours of the non-uniform model. This averaging does introduce a quantitative departure from the true cross-channel temperature field, as discussed in Appendix B, and so comparisons to full three-dimensional numerical solutions, and analogue experiments, would be valuable. In addition to the full three-dimensional temperature field, there are a number of physical processes neglected in this model. A more complete treatment would include the thermodynamics at the fissure walls (including solidification), viscous heating and dissolution of volatiles from the magma in response to the vertically decreasing pressure. In particular, the latter would both introduce buoyant forcing (Pioli *et al.* 2017) and also couple to the rheology of the fluid (Mader, Llewellin & Mueller 2013), which could further enhance localisation. Solidification is likely to eventually transition the localised channel flow into a circular conduit flow, although the impact of solidification on the onset of localisation is believed to be minor due to the relatively slow time scale on which it occurs (Wylie *et al.* 1999). Finally, here we considered only width variations that are aligned with the imposed pressure gradient. Such variations were considered most likely to support geometrically localised flow states; however, fissure geometries are typically more complex than this, and width variations in the flow direction are also common. It would therefore be valuable to explore the process of thermoviscous flow localisation in more general geometries.

5. Conclusion

We have studied the impact of a non-uniform fissure geometry on the localisation of a pressure-driven flow of fluid of a temperature-dependent viscosity, demonstrating that for topography aligned with the pressure gradient, relatively modest width variations and

sufficiently long wavelengths, the most dramatic localisation occurs in response to the interaction between the thermoviscosity and the fissure geometry, rather than through spontaneous localisation through viscous fingering. This geometry-dominated localisation occurs due to the wider region of the fissure remaining on the hot, fast branch of the planar solution curve, while the thinner region transitions to the cold, slow branch. The resulting system is stable over a range of pressure drops and exhibits flux localisation roughly an order of magnitude larger than that of the steady flow-focussed states obtained through the viscous fingering instability in planar geometries. Furthermore, the geometry-dominated localisation typically occurs at larger pressure drops, since the fingering instability only occurs once the system lies on the slow branch of the solution curve. We have demonstrated that geometric localisation is effective for conditions appropriate to a typical Hawaiian fissure eruption and operates over time scales that are consistent with observations. It seems very plausible, therefore, that the localisation of volcanic fissure eruptions is controlled in large part by the pre-existing geometry of the fissure. This highlights the value in methods to accurately measure fissure geometry, both post-eruption (for example, using robotics, see Parcheta *et al.* 2016, or from measurements of eroded feeder dykes, see Daniels *et al.* 2012) and ideally also syneruptively, to help constrain the future localisation of the eruption and inform hazard prediction and mitigation.

Declaration of interests. The authors report no conflict of interest.

Data availability statement. The data that support the findings of this study are available at https://doi.org/10.5281/zenodo.15660211 (Taylor-West & LLewellin 2025).

Appendix A. Numerical method

The governing equations in (2.22) are hyperbolic for $\mathcal{E}$ and elliptic for p. To avoid numerical instability of the nonlinear advection equation for $\mathcal{E}$, we discretise the system of equations via a first-order finite volume method, using upwinded fluxes in the z-direction. We define a grid with cell centres $\{\boldsymbol{x}_{i,j} = (x_i, z_j) : 1 \leqslant i \leqslant N, 1 \leqslant j \leqslant M\}$, and cell size Δx_i and Δz_j in the x- and z-directions respectively (see figure 12a). The cell-averaged values of $\mathcal{E}$ and p are written $E_{i,j}$ and $P_{i,j}$, respectively. Here, $x_1 = \Delta x_1/2$,
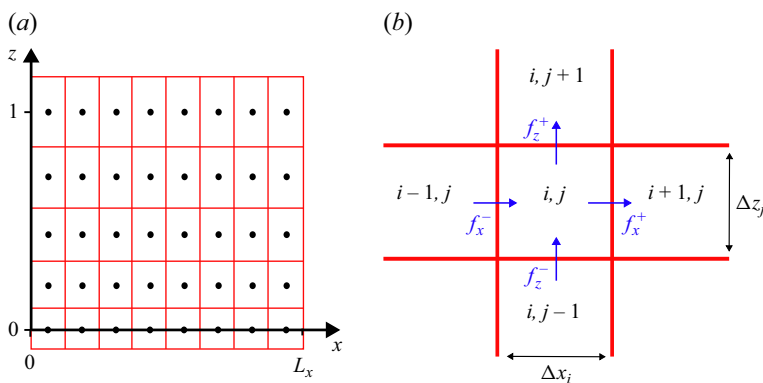

Figure 12. Diagrams of the finite volume grid used for the numerical solutions. (*a*) Diagram showing layout of cells. (*b*) Close up of a single stencil, showing direction of fluxes into and out of a given cell.

$x_N = L_x - \Delta x_N/2$, $z_1 = 0$ and $z_M = 1$. In general, the size in the x-direction is taken uniform,

$$\Delta x_i = \frac{L_x}{N_x}, \tag{A1}$$

whereas the grid is concentrated near the inflow, $z = 0$, in the z-direction to improve the resolution of the rapidly varying temperature here. In particular, we choose

$$\Delta z_j = \frac{2j}{M^2 - 1}, \tag{A2}$$

resulting in a quadratic spacing of the grid in this direction. We checked that solutions converge with N and M and chose a grid-size of $N = 500$ and $M = 200$ for the results reported here. For further verification of the numerical method, we employed our code with the averaging approach suggested by Wylie & Lister (1995) in a uniform geometry ($A = 0$) and confirmed that the resulting solution curve agreed closely with the results reported by Wylie & Lister (1995) and Morris (1996) for several values of the parameter γ.

We then discretise the equations in conservative form, writing the divergence terms as (for example)

$$\nabla \cdot (\mathcal{L}(\mathcal{E})\nabla p) = \frac{1}{\Delta x_i \Delta z_j} \left(f_x^+ + f_z^+ - f_x^- - f_z^- \right), \tag{A3}$$

where the fluxes are upwinded in the z-direction, giving

$$f_x^\pm \approx \Delta z_j \left. \left(\mathcal{L} \frac{\partial p}{\partial x} \right) \right|_{i+1/2, j} \approx \pm \Delta z_j \frac{\Delta x_{i\pm 1} \mathcal{L}(E_{i,j}) + \Delta x_i \mathcal{L}(E_{i\pm 1, j})}{\Delta x_i + \Delta x_{i\pm 1}} \left(\frac{P_{i\pm 1, j} - P_{i,j}}{(\Delta x_i + \Delta x_{i\pm 1})/2} \right), \tag{A4}$$

$$f_z^+ \approx \Delta x_i \mathcal{L}(E_{i,j}) \left. \frac{\partial p}{\partial z} \right|_{i, j+1/2} \approx \Delta x_i \mathcal{L}(E_{i,j}) \left(\frac{P_{i, j+1} - P_{i,j}}{(\Delta z_{j+1} + \Delta z_j)/2} \right), \tag{A5}$$

$$f_z^- \approx \Delta x_i \mathcal{L}(E_{i,j-1}) \left. \frac{\partial p}{\partial z} \right|_{i, j-1/2} \approx \Delta x_i \mathcal{L}(E_{i,j-1}) \left(\frac{P_{i, j} - P_{i,j-1}}{(\Delta z_j + \Delta z_{j-1})/2} \right). \tag{A6}$$

The same discretisation is used for the flux, $\mathcal{S}(\mathcal{E})\nabla p$, in the heat equation, simply replacing $\mathcal{L}$ with $\mathcal{S}$. We then flatten the grid via $\{\boldsymbol{x}_I = \boldsymbol{x}_{i,j} : \text{where } 1 \leqslant I \equiv N(j-1) + i \leqslant NM\}$ and obtain matrix equations for the vectors $\boldsymbol{E} = (E_{N+1}, E_{N+2}, \ldots, E_{N(M-1)})$ and $\boldsymbol{P} = (P_{N+1}, P_{N+2}, \ldots, P_{N(M-1)})$, where $E_I = \mathcal{E}(\boldsymbol{x}_I)$ and P_I defined similarly. Note that $E_1 = E_2 = \ldots = E_N = 0$ and $P_1 = P_2 = \ldots = P_N = 1$ by the boundary conditions at $z = 0$ and $P_{N(M-1)+1} = P_{N(M-1)+2} = \ldots = P_{NM} = 0$ by the boundary condition at $z = 1$. There is no equivalent boundary condition for $\mathcal{E}$ at $z = 1$, as appropriate given the hyperbolic nature of the equation, and so $E_{N(M-1)+1}, E_{N(M-1)+2}, \ldots, E_{NM}$ are never determined and do not enter the discretised equations due to the flux being up-winded in the z-direction (see A5). The discrete equations take the form

$$\frac{1}{\Pi} \dot{E}_I = A_{IJK} \mathcal{S}(E_J) P_K + a_{IJ} \mathcal{S}(E_J) + \frac{1}{\Pi} \mathcal{C}(E_I) \equiv F_I(\boldsymbol{E}, \boldsymbol{P}), \tag{A7}$$

$$0 = A_{IJK} \mathcal{L}(E_J) P_K + a_{IJ} \mathcal{L}(E_J) + b_{IJ} P_J \equiv G_I(\boldsymbol{E}, \boldsymbol{P}), \tag{A8}$$

where A_{IJK} is a sparse third-order tensor arising from the flux terms, and a_{IJ} and b_{IJ} are sparse matrices arising from the boundary conditions at $z = 1$ and $z = 0$, respectively.

1015 A18-28

The no-flux conditions at $x = 0, L_x$ are imposed by setting the fluxes, $f_x^{\pm}$, to zero, and thus these boundary conditions do not contribute additional terms to the equations.

Since the nonlinear functions of $\mathcal{E}$ are known analytically, the Jacobian of the system can be written down explicitly, given in block form by

$$J(E, P) = \left(\begin{array}{c|c} \partial F_I/\partial E_J & \partial F_I/\partial P_J \\ \hline \partial G_I/\partial E_J & \partial G_I/\partial P_J \end{array} \right) \tag{A9}$$

$$= \left(\begin{array}{c|c} A_{IJK}\mathcal{S}'(E_J)P_K + a_{IJ}\mathcal{S}'(E_J) + \hat{\delta}_{IJ}\mathcal{C}'(E_J)/\Pi & A_{IKJ}\mathcal{S}(E_K) \\ \hline A_{IJK}\mathcal{L}'(E_J)P_K + a_{IJ}\mathcal{L}'(E_J) & A_{IKJ}\mathcal{L}(E_K) + b_{IJ} \end{array} \right). \tag{A10}$$

Here, K is summed over, but I and J are not, and $\hat{\delta}_{IJ}$ represents the Kronecker-delta function. This Jacobian is used throughout the numerical procedures: for Newton iterations when solving directly for the steady state, $F_I(E, P) = G_I(E, P) = 0$; for time-stepping of the advection equation (A7) using a fourth-order, five-stage Rosenbrock method (Roche 1987); and in determining the linear stability of steady solutions to perturbations of the form $(E, P) = (E_0, P_0) + (E', P')e^{\sigma t}$, for which the modes and corresponding growth-rates are found from the generalised eigenvalue problem:

$$\sigma \begin{pmatrix} I & 0 \\ 0 & 0 \end{pmatrix} \begin{pmatrix} E' \\ P' \end{pmatrix} = \Pi J(E_0, P_0) \begin{pmatrix} E' \\ P' \end{pmatrix}. \tag{A11}$$

All of these procedures are carried out in MATLAB (The MathWorks Inc. 2023*a*,*b*), employing algorithms for large sparse arrays.

Appendix B. Comparison of averaging approaches

In this appendix, we make a quantitative comparison between the results of our heat-balance averaging and the approaches of Helfrich (1995), Wylie & Lister (1995) and Morris (1996). We first compare the critical values of γ in the uniform geometry, we denote γ_c, γ_{3d} and γ_{∞}, as discussed in §3.1. Not all of these are reported for the exponential viscosity function in all studies. Helfrich (1995) reports a value of $\gamma_c = 3.03$ for their averaging, while the unaveraged system first exhibits multiplicity of steady states at a larger value ($\gamma_c = 5.19$ reported by Morris 1996 and $\gamma_c = 5.25$ reported by Wylie & Lister 1995). Thus, the value of $\gamma_c = 4.8$, found using our heat balance averaging, agrees better with the value for the unaveraged case than when employing the Darcy averaging, but still underestimates the critical viscosity ratio. For the unaveraged model with the exponential viscosity model, $\gamma_{3d} \approx 5.5$ (see Morris 1996, figures 5 and 6) and $\gamma_{\infty} = 5.78$ (Morris 1996), compared with the values $\gamma_{3d} \approx 5.2$ and $\gamma_{\infty} \approx 5.4$ for our system. Thus, as well as reproducing the behaviour qualitatively, the heat balance averaging does not significantly underestimate the critical values of the viscosity ratio at which the system changes behaviour (compared with say the Darcy averaging of Helfrich 1995).

Nonetheless, the approximation of the temperature field by (2.10) does introduce quantitative differences from the unaveraged system. This is demonstrated in figure 13(*a*), which shows the steady-state solution curve for $\gamma = 5.5$, calculated with the Darcy averaging of Helfrich (1995), the unaveraged approach of Wylie & Lister (1995) and Morris (1996), and the heat balance method detailed in §2.1. All three approaches agree at low Π and Q, where the majority of the fissure has a uniform cold temperature across its width, but differ elsewhere. The origin of the discrepancies can be understood by considering the approximations to the temperature profile. Figure 13(*b*) shows example across-channel temperature profiles for the three models at the same average temperature.
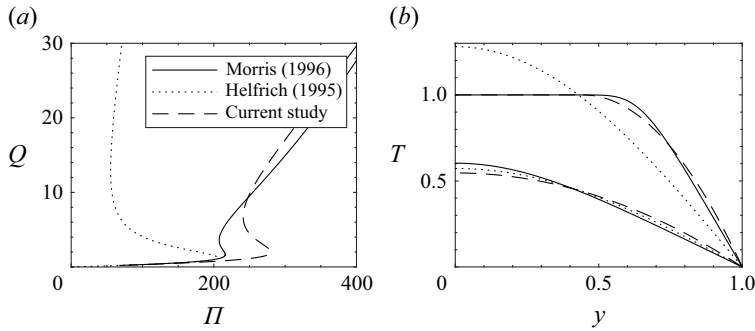
Figure 13. (*a*) Steady-state dimensionless flux per unit length, Q, against dimensionless pressure drop, Π, for the uniform geometry, $h = 1$, and $\gamma = 5.5$ (as in figure 2). Solution curves are shown for the unaveraged approach of Morris (1996) (solid), the Darcy averaging employed by Helfrich (1995) (dotted) and the heat balance averaging detailed in § 2.1 (dashed). (*b*) Example across-channel temperature profiles, $T(y)$. The solid curves show two temperature profiles that occur at different points along the channel in the unaveraged model of Morris (1996). These profiles were calculated using the numerical method detailed in Appendix B of Morris (1996), and are taken at the locations $s = 0.1$ (top) and $s = 0.6$ (bottom) in the notation of their appendix. Dashed lines show corresponding temperature profiles from the approximation (2.10), giving the same average temperature across the gap. The dotted lines show the sinusoidal profile giving the same average, as used by Helfrich (1995) in modelling the heat flux at the wall (but not the variation of viscosity across the channel).

When the fluid is hot and the temperature profile is significantly non-uniform across the channel, the averaging of Helfrich (1995) tends to underestimate the temperature gradient at the wall (since it does not account for thin thermal boundary layers). As a result, the material cools less quickly and the dimensionless pressure drop at which the slow branch joins the intermediate branch is underestimated by this averaging. More dramatically, the flux on the fast branch is significantly overestimated. By contrast, the parabolic approximation to the temperature profile, (2.10), tends to overestimate the heat flux to the walls, and so the fold bifurcations happen at larger Π than in the unaveraged system. The flux on the fast branch (large Π and Q) agrees with the unaveraged model much more closely than when employing the averaging of Helfrich (1995), since the variation of the viscosity across the channel is included in the model, and the assumed temperature profile is able to more closely represent the true profile when the fluid is at the eruption temperature across most of the channel, with thermal boundary layers at the walls. As discussed in § 3.3, the strength of geometrically driven flow focussing is largely controlled by the relative magnitude of fluxes on the fast and slow branches, and so capturing this is particularly important in the current study.

In figure 14, we include some results for a non-uniform geometry and the 'unaveraged' model of Wylie & Lister (1995) for comparison with the results of the heat balance averaging. Panels (*a*)–(*c*) show the steady-state curves for the sinusoidal geometries with $A = 0.05$ and $\lambda = 2$, 1 and 0.4, and $\gamma = 5.5$, to be compared with the middle column of figure 4, while panel (*d*) corresponds to figure 5(*c*). The qualitative behaviour is very similar, with the unstable middle branch of the solution curve being replaced with a stable, flow-focussed branch. The range of Π that is spanned by this branch is shorter and is shifted to lower values of Π, as anticipated from a comparison of the locations of the fold bifurcations for the uniform geometry (see figure 13*a*). The degree of flux focussing, indicated by the scaled surface flux ratio, $\tilde{Q}_r$, is also not as large as for the heat balance averaging, but is still significantly stronger than that obtained from steady fingered solutions, typically exceeding a factor of 4. We note that, since $5.5 < \gamma_\infty = 5.78$ for the unaveraged system (Morris 1996), at this value of γ, the region of the solution branch
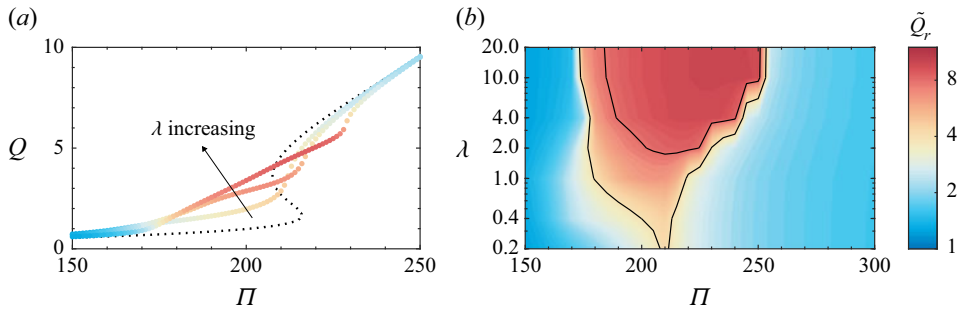
Figure 14. Example steady-state results for the 'unaveraged' model of Wylie & Lister (1995) with $\gamma = 5.5$ and the sinusoidal geometry with $A = 0.05$. (*a*) Steady-state solution curves, Q as a function of Π, as in figure 4, with colour corresponding to the scaled surface flux ratio, $\tilde{Q}_r$, as shown in the logarithmic colour bar on the right. The three coloured curves are for geometrical wavelengths, $\lambda = 0.4$, 1 and 2 (increasing in the direction shown) and the black dotted curve shows the steady-state solution curve for the uniform geometry, $A = 0$. The corresponding results for the heat balance averaging can be found in the middle curve of each panel in figure 4. (*b*) Contour plot of scaled surface flux ratio, $\tilde{Q}_r$, as a function of dimensionless pressure drop and wavelength, as in figure 5(*c*). The black contours are plotted at $\tilde{Q}_r = 4$ and 8. See table 2 for other parameters used in these solutions.

which becomes unstable to the fingering instability is rather limited. We were unable to find any steady flow-focussed states for the uniform geometry at this parameter value, with the unstable solutions instead continuing to evolve onto the fast branch, as observed by Wylie & Lister (1995). Thus, in this case, the non-uniform geometry provides a mechanism for the existence of steady flow-focussed solutions which are otherwise absent in the case of the uniform geometry. We further note that, in this case, there are no periodic solutions, which also relates to the absence of steady fingered states in the uniform geometry at this viscosity ratio, since the periodic orbits arise from oscillations between different fingered states (see § 3.4).

REFERENCES

ALLGOOD, C., LLEWELLIN, E.W., HUMPHREYS, M.C.S., MATHIAS, S.A., BROWN, R.J. & VYE-BROWN, C. 2024 Banding in the margins of basaltic dykes indicates pulsatory propagation during emplacement. *J. Geophys. Res.: Solid Earth* **129** (4), e2023JB028007.

ALLGOWER, E.L. & GEORG, K. 2003 *Introduction to Numerical Continuation Methods*. SIAM.

ANDERSON, K.R., SHEA, T., LYNN, K.J., MONTGOMERY-BROWN, E.K., SWANSON, D.A., PATRICK, M.R., SHIRO, B.R. & NEAL, C.A. 2024 The 2018 eruption of Kīlauea: insights, puzzles, and opportunities for volcano science. *Annu. Rev. Earth Planet. Sci.* **52** (1), 21–59.

AURADOU, H., DRAZER, G., HULIN, J.P. & KOPLIK, J. 2005 Permeability anisotropy induced by the shear displacement of rough fracture walls. *Water Resour. Res.* **41** (9), W09423.

BALMFORTH, N.J., CRASTER, R.V. & SASSI, R. 2004 Dynamics of cooling viscoplastic domes. *J. Fluid Mech.* **499**, 149–182.

BERNABEU, N., SARAMITO, P. & SMUTEK, C. 2016 Modelling lava flow advance using a shallow-depth approximation for three-dimensional cooling of viscoplastic flows. *Geol. Soc. Lond. Special Publications* **426** (1), 409–423.

BRODSKY, E.E., KIRKPATRICK, J.D. & CANDELA, T. 2016 Constraints from fault roughness on the scale-dependent strength of rocks. *Geology* **44** (1), 19–22.

BRUCE, P.M. & HUPPERT, H.E. 1989 Thermal control of basaltic fissure eruptions. *Nature* **342** (6250), 665–667.

CANDELA, T., RENARD, F., KLINGER, Y., MAIR, K., SCHMITTBUHL, J. & BRODSKY, E.E. 2012 Roughness of fault surfaces over nine decades of length scales. *J. Geophys. Res.: Solid Earth* **117** (B8), B08409.

DANIELS, K.A., KAVANAGH, J.L., MENAND, T. & SPARKS, R.S.J. 2012 The shapes of dikes: evidence for the influence of cooling and inelastic deformation. *GSA Bulletin* **124** (7-8), 1102–1112.

DELANEY, P.T. & POLLARD, D.D. 1982 Solidification of basaltic magma during flow in a dike. *Am. J. Sci.* **282** (6), 856–885.

DRAGONI, M. 1989 A dynamical model of lava flows cooling by radiation. *Bull. Volcanol.* **51** (2), 88–95.

EIBL, E.P.S., BEAN, C.J., JÓNSDÓTTIR, I., HÖSKULDSSON, A., THORDARSON, T., COPPOLA, D., WITT, T. & WALTER, T.R. 2017 Multiple coincident eruptive seismic tremor sources during the 2014–2015 eruption at Holuhraun, Iceland. *J. Geophys. Res.: Solid Earth* **122** (4), 2972–2987.

FRANCO-GÓMEZ, A., THOMPSON, A.B., HAZEL, A.L., JUEL, A. 2016 Sensitivity of Saffman–Taylor fingers to channel-depth perturbations. *J. Fluid Mech.* **794**, 343–368.

GIORDANO, D., RUSSELL, J.K. & DINGWELL, D.B. 2008 Viscosity of magmatic liquids: a model. *Earth Planet. Sci. Lett.* **271** (1), 123–134.

HELFRICH, K.R. 1995 Thermo-viscous fingering of flow in a thin gap: a model of magma flow in dikes and fissures. *J. Fluid Mech.* **305**, 219–238.

HOUGHTON, B.F., TISDALE, C.M., LLEWELLIN, E.W., TADDEUCCI, J., ORR, T.R., WALKER, B.H. & PATRICK, M.R. 2021 The birth of a Hawaiian fissure eruption. *J. Geophys. Res.: Solid Earth* **126** (1), e2020JB020903.

HYMAN, D.M.R., DIETTERICH, H.R. & PATRICK, M.R. 2022 Toward next-generation lava flow forecasting: development of a fast, physics-based lava propagation model. *J. Geophys. Res.: Solid Earth* **127** (10), e2022JB024998.

IDA, Y. 1992 Width change of a planar magma path: implication for the evolution and style of volcanic eruptions. *Phys. Earth Planet. Inter.* **74** (3), 127–138.

JONES, T.J. & LLEWELLIN, E.W. 2021 Convective tipping point initiates localization of basaltic fissure eruptions. *Earth Planet. Sci. Lett.* **553**, 116637.

JONES, T.J., LLEWELLIN, E.W., HOUGHTON, B.F., BROWN, R.J. & VYE-BROWN, C. 2017 Proximal lava drainage controls on basaltic fissure eruption dynamics. *Bull. Volcanol.* **79** (11), 81.

KILBURN, C.R.J. 2000 Lava flows and flow fields. In *The Encyclopedia of Volcanoes*, First edition (ed. H. SIGURDSSON, B. HOUGHTON, H. RYMER, J. STIX & S NCNUTT), pp. 291–305. Academic Press.

LAWLESS, J., HAZEL, A. & JUEL, A. 2024 Periodic dynamics in viscous fingering. *Proc. R. Soc. Lond. A: Math. Phys. Engng Sci.* **480**(2301), 20240164.

MADER, H.M., LLEWELLIN, E.W. & MUELLER, S.P. 2013 The rheology of two-phase magmas: a review and analysis. *J. Volcanol. Geotherm. Res.* **257**, 135–158.

MCBIRNEY, A.R. & MURASE, T. 1984 Rheological properties of magmas. *Annu. Rev. Earth Planet. Sci.* **12** (1984), 337–357.

MOORE, J.G. 2001 Density of basalt core from Hilo drill hole, Hawaii. *J. Volcanol. Geotherm. Res.* **112** (1), 221–230.

MORRIS, S.J.S. 1996 Stability of thermoviscous Hele–Shaw flow. *J. Fluid Mech.* **308**, 111–128.

MOYERS-GONZALEZ, M., HEWETT, J.N., CUSACK, D.R., KENNEDY, B.M. & SELLIER, M. 2023 Non-isothermal thin-film flow of a viscoplastic material over topography: critical Bingham number for a partial slump. *Theor. Comput. Fluid Dyn.* **37** (2), 151–172.

MÉHEUST, Y. & SCHMITTBUHL, J. 2000 Flow enhancement of a rough fracture. *Geophys. Res. Lett.* **27** (18), 2989–2992.

NEAL, C.A. *et al.* 2019 The 2018 rift eruption and summit collapse of Kīlauea Volcano. *Science* **363** (6425), 367–374.

PAILHA, M., HAZEL, A.L., GLENDINNING, P.A. & JUEL, A. 2012 Oscillatory bubbles induced by geometrical constraint. *Phys. Fluids* **24** (2), 021702.

PARCHETA, C., FAGENTS, S., SWANSON, D.A., HOUGHTON, B.F. & ERICKSEN, T. 2015 Hawaiian fissure fountains. In *Hawaiian Volcanoes*, pp. 369–391. American Geophysical Union (AGU).

PARCHETA, C.E., PAVLOV, C.A., WILTSIE, N., CARPENTER, K.C., NASH, J., PARNESS, A. & MITCHELL, K.L. 2016 A robotic approach to mapping post-eruptive volcanic fissure conduits. *J. Volcanol. Geotherm. Res.* **320**, 19–28.

PEARSON, J.R.A., SHAH, Y.T. & VIEIRA, E.S.A. 1973 Stability of non-isothermal flow in channels—I. Temperature dependent Newtonian fluid without heat generation. *Chem. Engng Sci.* **28** (11), 2079–2088.

PIOLI, L., AZZOPARDI, B.J., BONADONNA, C., BRUNET, M. & KUROKAWA, A.K. 2017 Outgassing and eruption of basaltic magmas: the effect of conduit geometry. *Geology* **45** (8), 759–762.

RICHTER, D.H., EATON, J.P., MURATA, K.J., AULT, W.U. & KRIVOY, H.L. 1970 Chronological narrative of the 1959–60 eruption of Kilauea Volcano, Hawaii. Report 537E. U.S. Geological Survey.

ROCHE, M. 1987 Rosenbrock methods for differential algebraic equations. *Numer. Math.* **52** (1), 45–63.

RONGO, R., LUPIANO, V., SPATARO, W., D'AMBROSIO, D., IOVINE, G. & CRISCI, G.M. 2016 Sciara: cellular automata lava flow modelling and applications in hazard prediction and mitigation. *Geol. Soc. Lond. Special Publications* **426** (1), 345–356.

SHAW, H.R. 1969 Rheology of Basalt in the melting range. *J. Petrol.* **10** (3), 510–535.

SIGURDSSON, H. 2000 Volcanic episodes and rates of volcanism. In *The Encyclopedia of Volcanoes*, First edition (ed. H. SIGURDSSON, B. HOUGHTON, H. RYMER, J STIX & S. MCNUTT), pp. 271–279. Academic Press.

SOLDATI, A., HOUGHTON, B.F. & DINGWELL, D.B. 2021 A lower bound on the rheological evolution of magmatic liquids during the 2018 Kilauea eruption. *Chem. Geol.* **576**, 120272.

SPERA, F.J., YUEN, D.A. & KIRSCHVINK, S.J. 1982 Thermal boundary layer convection in silicic magma chambers: effects of temperature-dependent rheology and implications for thermogravitational chemical fractionation. *J. Geophy. Res.: Solid Earth* **87** (B10), 8755–8767.

STROGATZ, S. 2015*a Nonlinear Dynamics and Chaos: With Applications to Physics, Biology, Chemistry, and Engineering*. 2nd edn. CRC Press.

STROGATZ, S. 2015*b Nonlinear Dynamics and Chaos: With Applications to Physics, Biology, Chemistry, and Engineering*, 2nd edn. CRC Press.

TAYLOR-WEST, J.J., LLEWELLIN, E.W. & LLEWELLIN, E.W. 2025 Figure data and scripts for Taylor-West, J. J. & Llewellin, E. W. (2025) Thermoviscous localisation of volcanic eruptions is enhanced by variations in fissure width. Zenodo. https://doi.org/10.5281/zenodo.15660211

The MathWorks Inc.2023*a* MATLAB version: 9.14.0 (r2023a). The MathWorks Inc.

The MathWorks Inc. 2023*b* Optimization toolbox version: 9.5 (r2023a). The MathWorks Inc.

THOMPSON, A B., JUEL, A. & HAZEL, A L. 2014 Multiple finger propagation modes in Hele–Shaw channels of variable depth. *J. Fluid Mech.* **746**, 123–164.

THORARINSSON, S., STEINTHÓRSSON, S., EINARSSON, TH, KRISTMANNSDÓTTIR, H. & OSKARSSON, N. 1973 The eruption on Heimaey, Iceland. *Nature* **241** (5389), 372–375.

THOREY, C. & MICHAUT, C. 2016 Elastic-plated gravity currents with a temperature-dependent viscosity. *J. Fluid Mech.* **805**, 88–117.

TILLING, R.I., CHRISTIANSEN, R.L., DUFFIELD, W.A., ENDO, E.T., HOLCOMB, R.T., KOYANAGI, R.Y., PETERSON, D.W. & UNGER, J.D. 1987 The 1972–1974 Mauna Ulu eruption, Kilauea Volcano: an example of quasi-steady-state magma transfer (Hawaii). *US Geol. Surv. Prof. Paper* **1350**, 405–469.

TROLL, V.R., DEEGAN, F.M., THORDARSON, T., TRYGGVASON, A., KRMÍČEK, L., MORELAND, W.M., LUND, B., BINDEMAN, I.N., HÖSKULDSSON, Á. & DAY, J.M.D. 2024 The Fagradalsfjall and Sundhnúkur fires of 2021-2024: A single magma reservoir under the Reykjanes Peninsula, Iceland? *Terra Nova* **36**, 447–456.

WALKER, G.P.L. 1986 Koolau dike complex, Oahu: intensity and origin of a sheeted-dike complex high in a Hawaiian volcanic edifice. *Geology* **14** (4), 310–313.

WHITEHEAD, J.A. & HELFRICH, K.R. 1991 Instability of flow with temperature-dependent viscosity: a model of magma dynamics. *J. Geophys. Res.: Solid Earth* **96** (B3), 4145–4155.

WYLIE, J.J., HELFRICH, K.R., DADE, B., LISTER, J.R. & SALZIG, J.F. 1999 Flow localization in fissure eruptions. *Bull. Volcanol.* **60** (6), 432–440.

WYLIE, J.J. & LISTER, J.R. 1995 The effects of temperature-dependent viscosity on flow in a cooled channel with application to basaltic fissure eruptions. *J. Fluid Mech.* **305**, 239–261.